ARTICLE

A Hermitian C^2 Differential Reproducing Kernel Interpolation Meshless Method for the 3D Microstructure-Dependent Static Flexural Analysis of Simply Supported and Functionally Graded Microplates

Chih-Ping Wu[*] and Ruei-Syuan Chang

Department of Civil Engineering, National Cheng Kung University, Tainan, 70101, Taiwan

*Corresponding Author: Chih-Ping Wu. Email: cpwu@mail.ncku.edu.tw

ABSTRACT

This work develops a Hermitian C^2 differential reproducing kernel interpolation meshless (DRKIM) method within the consistent couple stress theory (CCST) framework to study the three-dimensional (3D) microstructure-dependent static flexural behavior of a functionally graded (FG) microplate subjected to mechanical loads and placed under full simple supports. In the formulation, we select the transverse stress and displacement components and their first- and second-order derivatives as primary variables. Then, we set up the differential reproducing conditions (DRCs) to obtain the shape functions of the Hermitian C^2 differential reproducing kernel (DRK) interpolant's derivatives without using direct differentiation. The interpolant's shape function is combined with a primitive function that possesses Kronecker delta properties and an enrichment function that constituents DRCs. As a result, the primary variables and their first- and second-order derivatives satisfy the nodal interpolation properties. Subsequently, incorporating our Hermitian C^2 DRK interpolant into the strong form of the 3D CCST, we develop a DRKIM method to analyze the FG microplate's 3D microstructure-dependent static flexural behavior. The Hermitian C^2 DRKIM method is confirmed to be accurate and fast in its convergence rate by comparing the solutions it produces with the relevant 3D solutions available in the literature. Finally, the impact of essential factors on the transverse stresses, in-plane stresses, displacements, and couple stresses that are induced in the loaded microplate is examined. These factors include the length-to-thickness ratio, the material length-scale parameter, and the inhomogeneity index, which appear to be significant.

KEYWORDS

Consistent/modified couple stress theory; differential reproducing kernel methods; microplates; point collocation methods; static flexural; 3D microstructure-dependent analysis

1 Introduction

With the increasing demand for microstructures in industry and the rapid progress in material manufacturing technology, functionally graded (FG) structures have gradually shrunk from the macro scale to the micron scale. FG microstructures are gradually being used in cutting-edge technology fields, including thin films [1,2], micro-electro-mechanical systems [3,4], and atomic force microscopes [5,6]. Thus, developing an effective computational method to investigate the mechanical behavior of these microstructures has attracted considerable attention.

It is well-known that the mechanical behavior of FG macrostructures will be changed as their dimensions shrink from the macro-scale to the micro-scale [7]. The existing shell, plate, and beam theories based on the classical continuum mechanics (CCM) are inappropriate for use to analyze the dynamic and static responses of FG microshells, microplates, and microbeams due to the microstructure-dependent effect becoming significant. As a result, some non-CCM-based theoretical methods accounting for the microstructure-dependent impact have been proposed to investigate the mechanical behavior of microstructures. These theoretical methods include the couple stress theory (CST) [8,9], the strain gradient theory (SGT) [10,11], the doublet mechanics theory [12], the micropolar elasticity theory [13,14], and the nonlocal elasticity theory [15].

Hadjesfandiari et al. [16,17] and Yang et al. [18] established the consistent CST (CCST) and the modified CST (MCST) by assuming the couple-stress tensor is skew-symmetric and symmetric, respectively. As a result, instead of two material length-scale coefficients, which are required to study an elastic isotropic body's mechanical behavior when the original CST is employed, only one material length-scale coefficient is needed when the MCST/CCST is employed. This facilitates their future application.

Within the CCST/MCST framework, some two-dimensional (2D) shear deformation theories for investigating the microstructure-dependent mechanical behavior of FG microplates/microshells have been developed by assuming particular kinematics models *a priori*. Beni et al. [19] presented a microstructure-dependent classical shell theory on the basis of the MCST to determine an FG circular cylindrical microshell's smallest natural frequency and its corresponding wave number pair. Incorporating Mindlin's kinematics model into the MCST, Ma et al. [20] established a microstructure-dependent first-order shear deformation theory (FOSDT) to analyze a homogeneous isotropic microplate's flexural and free vibration behaviors. Arefi et al. [21] developed a novel shear deformation theory on the basis of the MCST to examine a three-layered microplate's stress and displacement, for which the microplate of interest consists of an exponentially graded (EG) core and two piezomagnetic face sheets. Based on Hamilton's principle combined with Reddy's kinematics model, Lei et al. [22] and Thai et al. [23] presented a microstructure-dependent refined shear deformation theory (RSDT) on the basis of the MCST to conduct an FG microplate's microstructure-dependent deformation and natural frequency behavior analyses. Kim et al. [24] developed a microstructure-dependent and MCSD-based third-order shear deformation theory (TOSDT) to investigate an FG microplate's static buckling, static flexural, and free vibration behaviors. Thai et al. [25] developed a microstructure-dependent sinusoidal shear deformation theory (SSDT) on the basis of the MCST to examine an FG microplate's static flexural and free vibration behaviors. Sobhy et al. [26] presented a microstructure-dependent and MCST-based trigonometric shear deformation theory (TSDT) with four primary variables for modeling an EG microplate's static buckling, static flexural, and free vibration characteristics resting on Pasternak's foundation.

Unlike these 2D microstructure-dependent and MCST-based shear deformation theories mentioned above, Wu et al. [27] established the unified microstructure-dependent shear deformation theories based on the CCST to study an FG/EG elastic microplate's mechanical behavior. Their results showed that the CCST and MCST solutions of deformation and natural frequency associated with out-of-plane vibration modes are almost identical when setting the value of MCST's material length-scale parameter at twice that of CCST's material length-scale parameter. However, their solutions of natural frequency associated with the in-plane vibration modes are slightly different.

Instead of the CCST and MCST, other non-CCM-based analytical and numerical methods, including the SGT, the differential quadrature method (DQM), the iso-geometric analysis technique (IGAT), etc., have also been employed to study an FG microplate's mechanical behavior. Incorporating

Kirchhoff-Love's kinematics model into the SGT, Deng et al. [28] established a non-CCM-based theory to determine an FG microplate's smallest natural frequency with variable thickness. Within the SGT framework, Balobanov et al. [29] presented a microstructure-dependent classical thin shell theory to investigate a circular cylindrical microscale shell's static flexural behavior. Integrating the advantages of the finite element method (FEM) and the DQM, Zhang et al. [30] developed a Hermitian C^1 four-node quadrilateral element for conducting a moderately thick microplate's mechanical behavior analysis. Integrating the MCST and the IGAT, Thanh et al. [31] established a seventh-order shear deformation theory for analyzing a porous FG microplate's microstructure-dependent nonlinear thermal stability behavior. Nguyen et al. [32] developed a computational approach for analyzing an FG microplate's geometrically nonlinear behavior on the basis of the IGAT and the RSDT. In conjunction with a modified nonlocal CST and the IGAT, Pham et al. [33] conducted an FG microplate's static flexural and free vibration characteristics analyses, where the microplate rested on an elastic foundation. Based on the CCST, Wu and his colleagues [34,35] established a semi-analytical Hermitian C^n FEM to conduct elastic and piezoelectric microscale plates'/shells' microstructure-dependent static and dynamic behavior analyses.

Meshless methods have also been employed to investigate a microscale structure's mechanical behavior. Incorporating Mindlin's kinematics model and radial basis functions into the MCST, Roque et al. [36] proposed a point collocation method for analyzing a homogeneous isotropic microplate's static flexural behavior. Incorporating HSDT's kinematics model into the MCST, Tran et al. [37] and Thai et al. [38] presented a moving Kriging interpolation meshless method to investigate an FG sandwich microplate's static buckling, static flexural, and free vibration characteristics. Nguyen et al. [39] incorporated a four-variable kinematics model into the MCST to develop a non-uniform rational B-splines (NURBS) meshless method, which was used to investigate an FG microplate's microstructure-dependent static buckling, static flexural, and free vibration behaviors. Finally, Thai et al. [40] employed the NURBS meshless method to conduct an FG microplate's static buckling and free vibration behavior analyses.

In their series of papers, Li et al. [41], Simkins et al. [42], Liu et al. [43], and Lu et al. [44] established the reproducing kernel element method to solve Galerkin weak forms of a system of higher order partial differential equations which are associated with Dirichlet boundary conditions.

Chen et al. [45] and Wang et al. [46] established the Hermitian C^1 and Lagrange C^0 differential reproducing kernel interpolation meshless (DRKIM) methods, respectively, for investigating laminated composite and FG macroscale structures' mechanical behavior. The novelty of these DRKIM methods is that the shape functions of the differential reproducing kernel (DRK) interpolant's derivatives are obtained by setting up the differential reproducing conditions (DRCs) without using direct differentiation, as is necessary for the conventional reproducing kernel interpolation and approximation methods [47]. It has been shown that the solutions obtained using these DRKIM methods closely agree with the available 3D solutions of macroscale plates, rather than those of microplates.

As we see in the strong form of the 3D CCST, the primary variables' highest order derivative is the third order for microplates, which differs from the first order designation for macroscale plates. This situation will reduce the accuracy of the early proposed Hermitian C^1 and Lagrangian C^0 DRKIM methods and slow down their convergence rate. To enhance these DRKIM methods' accuracy and speed up their convergence rate, in this paper, we aim to establish a Hermitian C^2 DRKIM method by making some modifications: the Hermitian C^2 DRK interpolant should satisfy the nodal interpolation properties and the continuity conditions up to primary variables' second-order derivatives at each sampling node. Moreover, we also aim to establish the Hermitian C^2 DRKIM

method, which is a point collocation method, by incorporating our Hermitian C^2 DRK interpolant into the strong form of the 3D CCST to carry out an FG microplate's 3D microstructure-dependent static flexural analysis. After validating the Hermitian C^2 DRKIM's accuracy using the relevant 3D solutions reported in the literature, we will carry out a parametric study for the FG microplate's 3D microstructure-dependent static flexural behavior to examine how the impact of essential factors affects the induced deformations, in-plane stresses, transverse stresses, and couple stresses, including the length-to-thickness ratio, the material length-scale parameter, and the inhomogeneity index.

2 The Hermitian C^2 DRKIM Method

2.1 The Hermitian C^2 DRK Interpolant

We consider n_p discrete sampling nodes placed at $\xi = \xi_1, \xi_2, \cdots, \xi_{np}$, respectively, in a natural coordinate system ξ, the values of which are $\xi_1 = -1$, $\xi_{np} = 1$, and the others are randomly selected between -1 and 1. The Hermitian C^2 DRK interpolant $f^h(\xi)$ and its first- and second-order derivatives, $df^h(\xi)/d\xi$ and $d^2 f^h(\xi)/d\xi^2$ (i.e., $\theta^h(\xi)$ and $\kappa^h(\xi)$), are required to satisfy the nodal interpolation properties. Thus, it is defined as

$$f^h(\xi) = \sum_{l=1}^{np} \left[N_l(\xi) f_l + \hat{N}_l(\xi) \theta_l + \overline{N}_l(\xi) \kappa_l \right]$$

$$= \sum_{l=1}^{np} \left\{ [\phi_l(\xi) + \psi_l(\xi)] f_l + \left[\hat{\phi}_l(\xi) + \hat{\psi}_l(\xi) \right] \theta_l + \left[\overline{\phi}_l(\xi) + \overline{\psi}_l(\xi) \right] \kappa_l \right\}, \tag{1}$$

where $N_l(\xi)$, $\hat{N}_l(\xi)$, and $\overline{N}_l(\xi)$ $(l = 1, 2, \ldots, n_p)$ denote the Hermitian C^2 DRK interpolant's shape functions at $\xi = \xi_l$; f_l, θ_l, and κ_l are the nodal values of $f^h(\xi)$, $\theta^h(\xi)$, and $\kappa^h(\xi)$ at $\xi = \xi_l$, respectively. $\psi_l(\xi)$, $\hat{\psi}_l(\xi)$, and $\overline{\psi}_l(\xi)$ $(l = 1, 2, \ldots, n_p)$ are the primitive functions for $f^h(\xi)$, $\theta^h(\xi)$, and $\kappa^h(\xi)$, respectively, which are selected to satisfy the Kronecker delta properties. The primitive functions chosen in this article are $\psi_l(\xi) = w_q(\xi)$, $\hat{\psi}_l(\xi) = (\xi - \xi_l) w_q(\xi)$, and $\overline{\psi}_l(\xi) = (\xi - \xi_l)^2 w_q(\xi)/2$, in which $w_q(\xi)$ is defined as a normalized eighth-degree (octic) polynomial with the support size $a_0 = (0.99) \min(|\xi_l - \xi_{l+1}|, |\xi_l - \xi_{l-1}|)$, such that these primitive functions and their first- and second-derivatives satisfy the Kronecker delta properties (i.e., $\psi_l(\xi_k) = \delta_{lk}$, $d\hat{\psi}_l(\xi_k)/d\xi = \delta_{lk}$, $d^2 \overline{\psi}_l(\xi_k)/d\xi^2 = \delta_{lk}$, $\hat{\psi}_l(\xi_k) = \overline{\psi}_l(\xi_k) = 0$, $d\psi_l(\xi_k)/d\xi = d\overline{\psi}_l(\xi_k)/d\xi = 0$, and $d^2 \psi_l(\xi_k)/d\xi^2 = d^2 \hat{\psi}_l(\xi_k)/d\xi^2 = 0$). The symbols $\phi_l(\xi)$, $\hat{\phi}_l(\xi)$, and $\overline{\phi}_l(\xi)$ $(l = 1, 2, \ldots, n_p)$ are defined as the enrichment functions for $f^h(\xi)$, $\theta^h(\xi)$, and $\kappa^h(\xi)$, respectively, which are determined by setting up the nth-order DRCs. In our Hermitian C^2 DRK interpolant, the enrichment functions are arranged as $\phi_l(\xi) = w_a(\xi - \xi_l) \mathbf{P}^T(\xi - \xi_l) \mathbf{b}_0^{c2}(\xi)$, $\hat{\phi}_l(\xi) = w_a(\xi - \xi_l) \hat{\mathbf{P}}^T(\xi - \xi_l) \mathbf{b}_0^{c2}(\xi)$, and $\overline{\phi}_l(\xi) = w_a(\xi - \xi_l) \overline{\mathbf{P}}^T(\xi - \xi_l) \mathbf{b}_0^{c2}(\xi)$, in which $\mathbf{b}_0^{c2}(\xi)$ and $w_a(\xi - \xi_l)$ denote the undetermined function vector and a Gaussian function, respectively, and

$$\mathbf{P}^T(\xi - \xi_l) = \left\{ 1 \quad (\xi - \xi_l) \quad (\xi - \xi_l)^2 \quad \cdots \quad (\xi - \xi_l)^n \right\}, \tag{2}$$

$$\hat{\mathbf{P}}^T(\xi - \xi_l) = (-1) d\mathbf{P}^T(\xi - \xi_l)/d(\xi - \xi_l) = d\mathbf{P}^T(\xi - \xi_l)/d\xi_l$$

$$= \left\{ 0, -1, -2(\xi - \xi_l), -3(\xi - \xi_l)^2, \cdots, -n(\xi - \xi_l)^{n-1} \right\}, \tag{3}$$

$$\overline{\mathbf{P}}^T(\xi - \xi_l) = (-1)^2 d^2 \mathbf{P}^T(\xi - \xi)/d(\xi - \xi_l)^2 = d^2 \mathbf{P}^T(\xi - \xi_l)/d\xi_l^2$$

$$= \left\{ 0, 0, 2, 6(\xi - \xi_l), \cdots, n(n-1)(\xi - \xi_l)^{n-2} \right\}. \tag{4}$$

In order to determine the undetermined function vector $\mathbf{b}_0^{c1}(z)$, we select the complete nth-order polynomials as the basis functions that are to be reproduced and set up $(n+1)$ DRCs as follows:

$$\sum_{l=1}^{np} \left\{ [\phi_l(\xi) + \psi_l(\xi)] \xi_l^m + \left[\hat{\phi}_l(\xi) + \hat{\psi}_l(\xi)\right] m \xi_l^{m-1} + \left[\overline{\phi}_l(\xi) + \overline{\psi}_l(\xi)\right] m(m-1)\xi_l^{m-2} \right\} = \xi^m$$

$$m = 0, 1, \cdots, n. \tag{5}$$

Eq. (5) can be rearranged in the following explicit forms:

$$m = 0: \quad \sum_{l=1}^{np} [\phi_l(\xi) + \psi_l(\xi)] = 1 \Rightarrow \sum_{l=1}^{np} \phi_l(\xi) = 1 - \sum_{l=1}^{np} \psi_l(\xi), \tag{6}$$

$$m = 1: \quad \sum_{l=1}^{np} [\phi_l(\xi) + \psi_l(\xi)]\xi_l + \sum_{l=1}^{np} \left[\hat{\phi}_l(\xi) + \hat{\psi}_l(\xi)\right] = \xi$$

$$\Rightarrow \sum_{l=1}^{np} (\xi - \xi_l)\,\phi_l(\xi) + \sum_{l=1}^{np} (-1)\hat{\phi}_l(\xi) = -\sum_{l=1}^{np} (\xi - \xi_l)\,\psi_l(\xi) - \sum_{l=1}^{np} (-1)\hat{\psi}_l(\xi), \tag{7}$$

$$m = 2 \quad \sum_{l=1}^{np} [\phi_l(\xi) + \psi_l(\xi)]\xi_l^2 + \sum_{l=1}^{np} \left[\hat{\phi}_l(\xi) + \hat{\psi}_l(\xi)\right](2\xi_l) + \sum_{l=1}^{np} \left[\overline{\phi}_l(\xi) + \overline{\psi}_l(\xi)\right](2) = \xi^2$$

$$\Rightarrow \sum_{l=1}^{np} (\xi - \xi_l)^2 \phi_l(\xi) + \sum_{l=1}^{np} (-2)(\xi - \xi_l)\,\hat{\phi}_l(\xi) + \sum_{l=1}^{np} 2\overline{\phi}_l(\xi) \tag{8}$$

$$= -\sum_{l=1}^{np} (\xi - \xi_l)^2 \psi_l(\xi) - \sum_{l=1}^{np} (-2)(\xi - \xi_l)\,\hat{\psi}_l(\xi) - \sum_{l=1}^{np} 2\overline{\psi}_l(\xi),$$

$$\vdots$$

$$m = n: \sum_{l=1}^{np} [\phi_l(\xi) + \psi_l(\xi)]\xi_l^n + \sum_{l=1}^{np} \left[\hat{\phi}_l(\xi) + \hat{\psi}_l(\xi)\right]\left(n\xi_l^{n-1}\right) + \sum_{l=1}^{np} \left[\overline{\phi}_l(\xi) + \overline{\psi}_l(\xi)\right]\left[n(n-1)\xi_l^{n-2}\right] = \xi^n$$

$$\Rightarrow \sum_{l=1}^{np} (\xi - \xi_l)^n \phi_l(\xi) + \sum_{l=1}^{np} (-n)(\xi - \xi_l)^{n-1}\hat{\phi}_l(\xi) + \sum_{l=1}^{np} (n)(n-1)(\xi - \xi_l)^{n-2}\overline{\phi}_l(\xi) \tag{9}$$

$$= -\sum_{l=1}^{np} (\xi - \xi_l)^n \psi_l(\xi) - \sum_{l=1}^{np} (-n)(\xi - \xi_l)^{n-1}\hat{\psi}_l(\xi) - \sum_{l=1}^{np} (n)(n-1)(\xi - \xi_l)^{n-2}\overline{\psi}_l(\xi).$$

We rewrite Eqs. (6)–(9) in matrix form as follows:

$$\sum_{l=1}^{np} \mathbf{P}(\xi - \xi_l)\,\phi_l(\xi) + \sum_{l=1}^{np} \hat{\mathbf{P}}(\xi - \xi_l)\,\hat{\phi}_l(\xi) + \sum_{l=1}^{np} \overline{\mathbf{P}}(\xi - \xi_l)\,\overline{\phi}_l(\xi)$$

$$= \mathbf{P}(0) - \sum_{l=1}^{np} \mathbf{P}(\xi - \xi_l)\,\psi_l(\xi) - \sum_{l=1}^{np} \hat{\mathbf{P}}(\xi - \xi_l)\,\hat{\psi}_l(\xi) - \sum_{l=1}^{np} \overline{\mathbf{P}}(\xi - \xi_l)\,\overline{\psi}_l(\xi), \tag{10}$$

where $\mathbf{P}(\mathbf{0}) = \begin{bmatrix} 1 & 0 & 0 & \cdots & 0 \end{bmatrix}^T$.

We substitute the enrichment functions into the DRCs to yield the following expression for the undetermined function vector $\mathbf{b}_0^{c2}(\xi)$:

$$\mathbf{b}_0^{c2}(\xi) = \mathbf{A}_{c2}^{-1}(\xi)\left[\mathbf{P}(0) - \sum_{l=1}^{np} \mathbf{P}(\xi - \xi_l)\,\psi_l(\xi) - \sum_{l=1}^{np} \hat{\mathbf{P}}(\xi - \xi_l)\,\hat{\psi}_l(\xi) - \sum_{l=1}^{np} \overline{\mathbf{P}}(\xi - \xi_l)\,\overline{\psi}_l(\xi)\right], \tag{11}$$

where $\mathbf{A}_{c2}(\xi) = \sum_{l=1}^{np} [\mathbf{P}(\xi - \xi_l)\,w_a(\xi - \xi_l)\,\mathbf{P}^T(\xi - \xi_l) + \hat{\mathbf{P}}(\xi - \xi_l)\,w_a(\xi - \xi_l)\,\hat{\mathbf{P}}^T(\xi - \xi_l) + \overline{\mathbf{P}}(\xi - \xi_l)$
$w_a(\xi - \xi_l)\,\overline{\mathbf{P}}^T(\xi - \xi_l)]$.

We substitute Eq. (11) into Eq. (1) to yield the shape functions of the Hermitrian C^2 DRK interpolant as follows:

$$N_l(\xi) = \phi_l(\xi) + \psi_l(\xi) \qquad (l = 1, 2, \ldots, n_p), \tag{12}$$

$$\hat{N}_l(\xi) = \hat{\phi}_l(\xi) + \hat{\psi}_l(\xi) \qquad (l = 1, 2, \ldots, n_p), \tag{13}$$

$$\overline{N}_l(\xi) = \overline{\phi}_l(\xi) + \overline{\psi}_l(\xi) \qquad (l = 1, 2, \ldots, n_p), \tag{14}$$

where $\phi_l(\xi) = w_a(\xi - \xi_l)\,\mathbf{P}^T(\xi - \xi_l)\,\mathbf{b}_0^{c2}(\xi)$,

$$\hat{\phi}_l(\xi) = w_a(\xi - \xi_l)\,\hat{\mathbf{P}}^T(\xi - \xi_l)\,\mathbf{b}_0^{c2}(\xi),$$

$$\overline{\phi}_l(\xi) = w_a(\xi - \xi_l)\,\overline{\mathbf{P}}^T(\xi - \xi_l)\,\mathbf{b}_0^{c2}(\xi).$$

Eq. (11) shows that the enrichment functions vanish at all the sampling points (i.e., $\phi_l(\xi_k) = \hat{\phi}_l(\xi_k) = \overline{\phi}_l(\xi_k) = 0$, for all l and $k = 1, 2, \ldots, n_p$). When we select the primitive functions mentioned above for $f^h(\xi)$, such that $\psi_l(\xi_k) = \delta_{lk}$, $\hat{\psi}_l(\xi_k) = 0$, and $\overline{\psi}_l(\xi_k) = 0$ *a priori*, the shape functions will satisfy the Kronecher delta properties, which are $N_l(\xi_k) = \delta_{lk}$, $\hat{N}_l(\xi_k) = 0$, and $\overline{N}_l(\xi_k) = 0$

2.2 The Hermitian C2 DRK Interpolant's Derivatives

The Hermitian C^2 DRK interpolant $f^h(\xi)$ in Eq. (1) has the first-order derivative with respect to ξ:

$$\frac{df^h(\xi)}{d\xi} = \sum_{l=1}^{n_p} \left[N_l^{(1)}(\xi) f_l + \hat{N}_l^{(1)}(\xi)\,\theta_l + \overline{N}_l^{(1)}(\xi)\,\kappa_l \right]$$

$$= \sum_{l=1}^{n_p} \left[\left(\phi_l^{(1)}(\xi) + \psi_l^{(1)}(\xi)\right) f_l + \left(\hat{\phi}_l^{(1)}(\xi) + \hat{\psi}_l^{(1)}(\xi)\right)\,\theta_l + \left(\overline{\phi}_l^{(1)}(\xi) + \overline{\psi}_l^{(1)}(\xi)\right)\,\kappa_l \right], \tag{15}$$

where $N_l^{(1)}(\xi)$, $\hat{N}_l^{(1)}(\xi)$, and $\overline{N}_l^{(1)}(\xi)$ $(l = 1, 2, \ldots, n_p)$ are the shape functions of the Hermitian C^2 DRK interpolant's first-order derivative at the node $\xi = \xi_l$, which satisfy the Kronecker delta properties; $\psi_l^{(1)}(\xi)$, $\hat{\psi}_l^{(1)}(\xi)$, and $\overline{\psi}_l^{(1)}(\xi)$ $(l = 1, 2, \ldots, n_p)$ are primitive functions' first-order derivatives (i.e., $\psi_l^{(1)}(\xi) = d\psi_l(\xi)/d\xi$, $\hat{\psi}_l^{(1)}(\xi) = d\hat{\psi}_l(\xi)/d\xi$, and $\overline{\psi}_l^{(1)}(\xi) = d\overline{\psi}_l(\xi)/d\xi$); and $\phi_l^{(1)}(\xi)$, $\hat{\phi}_l^{(1)}(\xi)$, and $\overline{\phi}_l^{(1)}(\xi)$ $(l = 1, 2, \ldots, n_p)$ denote enrichment functions' first-order derivatives, which are obtained by imposing the nth-order DRCs, and are expressed as $\phi_l^{(1)}(\xi) = w_a(\xi - \xi_l)\,\mathbf{P}^T(\xi - \xi_l)\,\mathbf{b}_1^{c2}(\xi)$, $\hat{\phi}_l^{(1)}(\xi) = w_a(\xi - \xi_l)\,\hat{\mathbf{P}}^T(\xi - \xi_l)\,\mathbf{b}_1^{c2}(\xi)$, and $\overline{\phi}_l^{(1)}(\xi) = w_a(\xi - \xi_l)\,\overline{\mathbf{P}}^T(\xi - \xi_l)\,\mathbf{b}_1^{c2}(\xi)$, for which $\mathbf{b}_1^{c2}(\xi)$ is the undetermined function vector.

In order to determine the undetermined functions $\mathbf{b}_1^{c2}(\xi)$ in Eq. (15), again, we select the complete nth-order polynomials as the basis functions to be reproduced and set up $(n + 1)$ DRCs as follows:

$$\sum_{l=1}^{n_p} \left\{ \left[\phi_l^{(1)}(\xi) + \psi_l^{(1)}(\xi)\right]\xi_l^m + \left[\hat{\phi}_l^{(1)}(\xi) + \hat{\psi}_l^{(1)}(\xi)\right] m\,\xi_l^{m-1} + \left[\overline{\phi}_l^{(1)}(\xi) + \overline{\psi}_l^{(1)}(\xi)\right] m\,(m-1)\,\xi_l^{m-2} \right\}$$

$$= m\,\xi^{m-1}, \tag{16}$$

where $m = 0, 1, 2, \cdots, n$.

We rearrange Eq. (16) in the explicit forms as follows:

$$m = 0: \quad \sum_{l=1}^{np} \left[\phi_l^{(1)}(\xi) + \psi_l^{(1)}(\xi) \right] = 0 \quad \Rightarrow \sum_{l=1}^{np} \phi_l^{(1)}(\xi) = -\sum_{l=1}^{np} \psi_l^{(1)}(\xi),$$

(17)

$$m = 1: \sum_{l=1}^{np} \left[\phi_l^{(1)}(\xi) + \psi_l^{(1)}(\xi) \right] \xi_l + \sum_{l=1}^{np} \left[\hat{\phi}_l^{(1)}(\xi) + \hat{\psi}_l^{(1)}(\xi) \right] = 1$$

$$\Rightarrow \sum_{l=1}^{np} (\xi - \xi_l) \phi_l^{(1)}(\xi) + \sum_{l=1}^{np} (-1) \hat{\phi}_l^{(1)}(\xi) = -1 - \sum_{l=1}^{np} (\xi - \xi_l) \psi_l^{(1)}(\xi) - \sum_{l=1}^{np} (-1) \hat{\psi}_l^{(1)}(\xi),$$

(18)

$$m = 2: \sum_{l=1}^{np} \left[\phi_l^{(1)}(\xi) + \psi_l^{(1)}(\xi) \right] \xi_l^2 + \sum_{l=1}^{np} \left[\hat{\phi}_l^{(1)}(\xi) + \hat{\psi}_l^{(1)}(\xi) \right] (2\xi_l) + \sum_{l=1}^{np} \left[\overline{\phi}_l^{(1)}(\xi) + \overline{\psi}_l^{(1)}(\xi) \right] (2) = 2\xi$$

$$\Rightarrow \sum_{l=1}^{np} (\xi - \xi_l)^2 \phi_l^{(1)}(\xi) + \sum_{l=1}^{np} (-2)(\xi - \xi_l) \hat{\phi}_l^{(1)}(\xi) + \sum_{l=1}^{np} (2) \overline{\phi}_l^{(1)}(\xi)$$

$$= -\sum_{l=1}^{np} (\xi - \xi_l)^2 \psi_l^{(1)}(\xi) - \sum_{l=1}^{np} (-2)(\xi - \xi_l) \hat{\psi}_l^{(1)}(\xi) - \sum_{l=1}^{np} (2) \overline{\psi}_l^{(1)}(\xi),$$

(19)

$$\vdots$$

$$m = n: \sum_{l=1}^{np} \left[\phi_l^{(1)}(\xi) + \psi_l^{(1)}(\xi) \right] \xi_l^n + \sum_{l=1}^{np} \left[\hat{\phi}_l^{(1)}(\xi) + \hat{\psi}_l^{(1)}(\xi) \right] n\xi_l^{n-1} + \sum_{l=1}^{np} \left[\overline{\phi}_l^{(1)}(\xi) + \overline{\psi}_l^{(1)}(\xi) \right] n(n-1)\xi_l^{n-2}$$

$$= n\xi^{n-1} \Rightarrow \sum_{l=1}^{np} (\xi - \xi_l)^n \phi_l^{(1)}(\xi) + \sum_{l=1}^{np} (-n)(\xi - \xi_l)^{n-1} \hat{\phi}_l^{(1)}(\xi) + \sum_{l=1}^{np} (n)(n-1)(\xi - \xi_l)^{n-2} \overline{\phi}_l^{(1)}(\xi)$$

$$= -\sum_{l=1}^{np} (\xi - \xi_l)^n \psi_l^{(1)}(\xi) - \sum_{l=1}^{np} (-n)(\xi - \xi_l)^{n-1} \hat{\psi}_l^{(1)}(\xi) - \sum_{l=1}^{np} n(n-1)(\xi - \xi_l)^{n-2} \overline{\psi}_l^{(1)}(\xi).$$

(20)

We rewrite the above Eqs. (17)–(20) in matrix form as follows:

$$\sum_{l=1}^{np} \mathbf{P}(\xi - \xi_l) \phi_l^{(1)}(\xi) + \sum_{l=1}^{np} \hat{\mathbf{P}}(\xi - \xi_l) \hat{\phi}_l^{(1)}(\xi) + \sum_{l=1}^{np} \overline{\mathbf{P}}(\xi - \xi_l) \overline{\phi}_l^{(1)}(\xi)$$

$$= \hat{\mathbf{P}}(0) - \sum_{l=1}^{np} \mathbf{P}(\xi - \xi_l) \psi_l^{(1)}(\xi) - \sum_{l=1}^{np} \hat{\mathbf{P}}(\xi - \xi_l) \hat{\psi}_l^{(1)}(\xi) - \sum_{l=1}^{np} \overline{\mathbf{P}}(\xi - \xi_l) \overline{\psi}_l^{(1)}(\xi),$$

(21)

where $\hat{\mathbf{P}}(0) = d\mathbf{P}(0)/d\xi_l = \begin{bmatrix} 0 & -1 & 0 & \cdots & 0 \end{bmatrix}^T$.

We substitute the enrichment functions into the DRCs to yield the undetermined function vector $\mathbf{b}_1^{c2}(\xi)$ as follows:

$$\mathbf{b}_1^{c2}(\xi) = \mathbf{A}_{c2}^{-1}(\xi) \left[\hat{\mathbf{P}}(0) - \sum_{l=1}^{np} \mathbf{P}(\xi - \xi_l) \psi_l^{(1)}(\xi) - \sum_{l=1}^{np} \hat{\mathbf{P}}(\xi - \xi_l) \hat{\psi}_l^{(1)}(\xi) - \sum_{l=1}^{np} \overline{\mathbf{P}}(\xi - \xi_l) \overline{\psi}_l^{(1)}(\xi) \right].$$ (22)

We substitute Eq. (22) into Eq. (15) to obtain the shape functions of the Hermitian C^2 DRK interpolant's first-order derivatives as follows:

$$N_l^{(1)}(\xi) = \phi_l^{(1)}(\xi) + \psi_l^{(1)}(\xi) \qquad (l = 1, 2, \ldots, n_p),$$

(23)

$$\hat{N}_l^{(1)}(\xi) = \hat{\phi}_l^{(1)}(\xi) + \hat{\psi}_l^{(1)}(\xi) \qquad (l = 1, 2, \ldots, n_p), \tag{24}$$

$$\overline{N}_l^{(1)}(\xi) = \overline{\phi}_l^{(1)}(\xi) + \overline{\psi}_l^{(1)}(\xi) \qquad (l = 1, 2, \ldots, n_p), \tag{25}$$

where $\phi_l^{(1)}(\xi) = w_a(\xi - \xi_l) \mathbf{P}^T(\xi - \xi_l) \mathbf{b}_1^{c2}(\xi)$, $\hat{\phi}_l^{(1)}(\xi) = w_a(\xi - \xi_l) \hat{\mathbf{P}}^T(\xi - \xi_l) \mathbf{b}_1^{c2}(\xi)$, $\overline{\phi}_l^{(1)}(\xi) = w_a(\xi - \xi_l) \overline{\mathbf{P}}^T(\xi - \xi_l) \mathbf{b}_1^{c2}(\xi)$.

From Eqs. (23)–(25), it can be seen that the values of the enrichment functions' first-order derivatives at all sampling nodes are zero (i.e., $\phi_l^{(1)}(\xi_k) = \hat{\phi}_l^{(1)}(\xi_k) = \overline{\phi}_l^{(1)}(\xi_k) = 0$). Subsequently, suppose we select the first-order primitive functions for $df^h(\xi)/d\xi$ such that $\psi_l^{(1)}(\xi_k) = 0$, $\hat{\psi}_l^{(1)}(\xi_k) = \delta_{lk}$, and $\overline{\psi}_l^{(1)}(\xi_k) = 0$, *a priori*. Finally, the above shape functions satisfy the Kronecker delta properties (i.e., $N_l^{(1)}(\xi_k) = 0$, $\hat{N}_l^{(1)}(\xi_k) = \delta_{lk}$, and $\overline{N}_l^{(1)}(\xi_k) = 0$).

Similarly, the above derivation procedure can proceed to the rth-order derivative of the Hermitian C^2 DRK interpolant $f^h(\xi)$, which is thus expressed in Appendix A.

2.3 Weight Functions and Primitive Functions

In implementing our Hermitian C^2 DRKIM method, we must select the weight function and the primitive function in advance. This work uses the normalized Gaussian function as the weight function, which is expressed as follows [47]:

$$\text{Normalized Gaussian function: } w_a(s) = \begin{cases} \dfrac{e^{-(s/\alpha)^2} - e^{-(1/\alpha)^2}}{1 - e^{-(1/\alpha)^2}} & \text{for } s \leq 1 \\ 0 & \text{for } s > 1, \end{cases} \tag{26}$$

where $s = |\xi - \xi_l|/a_l$, in which a_l denotes the support size at the reference sampling point l, and the value of α is set at $\alpha = 0.3$.

As mentioned above, we define the primitive functions for the Hermitian C^2 DRK interpolant as $\psi_l(\xi) = w_q(\xi)$, $\hat{\psi}_l(\xi) = (\xi - \xi_l) w_q(\xi)$, and $\overline{\psi}_l(\xi) = (\xi - \xi_l)^2 w_q(\xi)/2$, respectively, for which $w_q(\xi)$ is a normalized eighth-degree (octic) polynomial, which is given as follows [47]:

$$w_q(s) = \begin{cases} -3s^8 + 8s^6 - 6s^4 + 1 & \text{for } s \leq 1 \\ 0 & \text{for } s > 1, \end{cases} \tag{27}$$

where $s = |\xi - \xi_l|/a_0$, in which a_0 is defined as $a_0 = (0.99) \min(|\xi_l - \xi_{l+1}|, |\xi_l - \xi_{l-1}|)$ to ensure the Kronecker delta properties are satisfied (i.e., $\psi_l(\xi = \xi_k) = \delta_{lk}$, $d\hat{\psi}_l(\xi_k)/d\xi = \delta_{lk}$, and $d^2\overline{\psi}_l(\xi_k)/d\xi^2 = \delta_{lk}$).

It is noticed that for a meshless method, the support size a_l for the selected weight function $w_a(\xi)$ will not be a very small value, often resulting in numerical errors; whereas, it also has to be small enough to preserve the meshless method's local character due to an increase in the support size also resulting in numerical errors. Chen et al. [45] and Wang et al. [46] thus recommended a compromise range of the value of a_l to ensure the Hermitian C^1 and Lagrange C^0 DRKIM methods' accuracy and convergence rate. It has been recommended as follows: In the case of a uniform sampling node distribution, the appropriate value of a_l is $a_l = (n + 0.1)\Delta\xi$, where $\Delta\xi$ denotes the spacing between the adjacent nodes, and the value of a_l is constant for each node. In the case of a randomly scattered node distribution, the appropriate value of a_l is selected to include $(2n + 1)$ nodes and the value of a_l is variable for each node. This guidance is adopted in this paper.

To have a clear picture related to how the values of these shape functions vary in the natural coordinate, in Fig. 1a–c, we consider a case of 11 sampling nodes with uniform spacing and present the

distributions of the enrichment function ($\psi_6(\xi)$), the primitive function ($\phi_6(\xi)$), and the shape function ($N_6(\xi)$) of node 6 along the natural coordinate axis, respectively, for which $N_6(\xi) = \phi_6(\xi) + \psi_6(\xi)$. It can be seen in Fig. 1a–c that the Kronecker delta properties, $\psi_6(\xi_i) = \delta_{i6}$ and $N_6(\xi_i) = \delta_{i6}$ $(i = 1 - 11)$, are satisfied, and $\phi_6(\xi_i) = 0$ $(i = 1 - 11)$. Furthermore, in Fig. 2, we present the distribution of each sampling node's shape function along the natural coordinate axis, i.e., $N_i(\xi)$ $(i = 1 - 11)$. Again, each shape function is shown to satisfy the Kronecker delta properties and localize in a region of the support size.
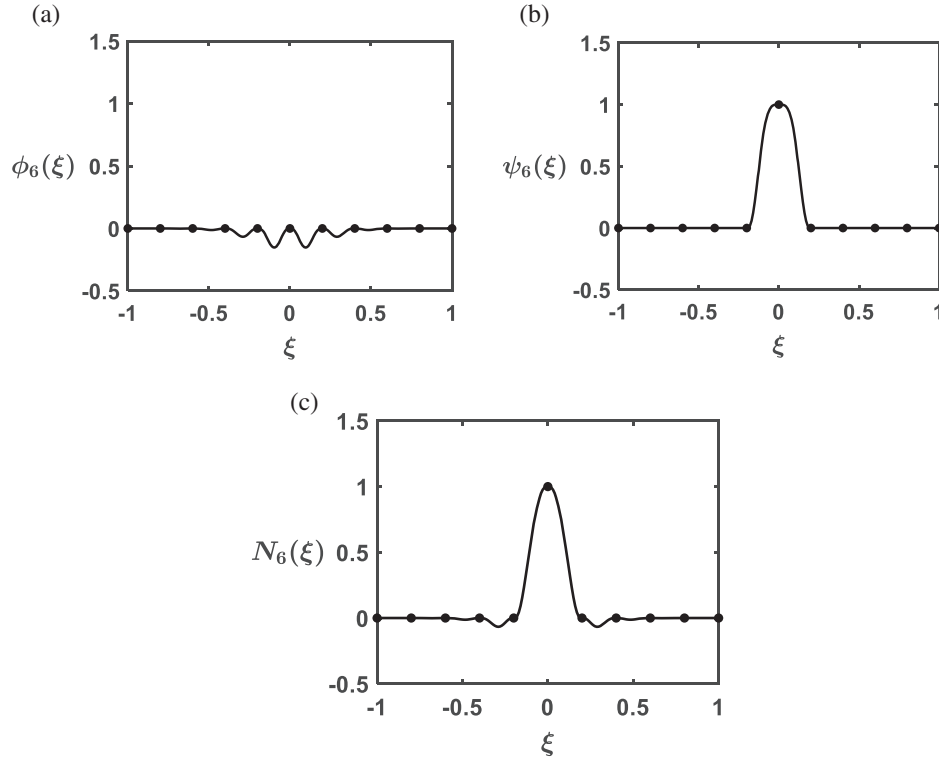
Figure 1: Distributions of (a) the enrichment function, (b) the primitive function, and (c) the shape function of node 6 in the natural coordinate in the case of $n_p = 11$ with uniform spacing
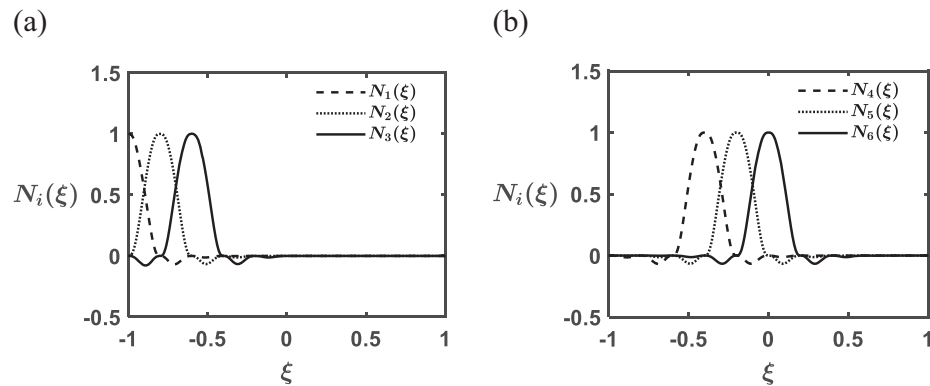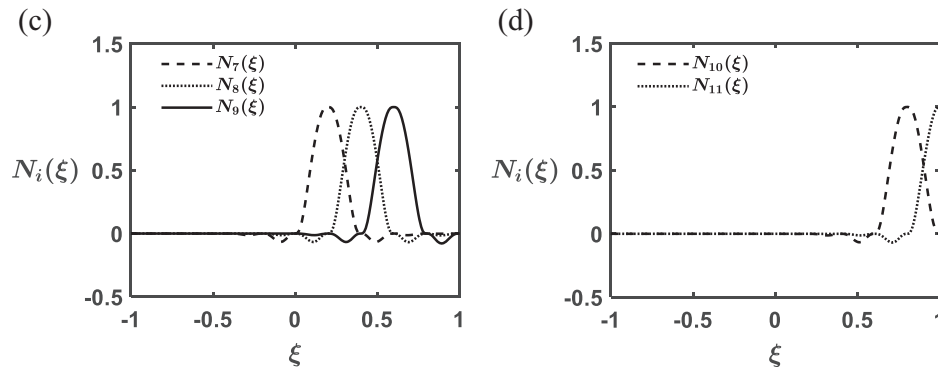
Figure 2: (Continued)

Figure 2: Distributions of the shape functions (a) (i = 1–3), (b) (i = 4–6), (c) (i = 7–9), and (d) (i = 10 and 11), in the natural coordinate in the case of $np = 11$ with uniform spacing

3 3D Microstructure-Dependent Static Flexural Analysis of FG/EG Microplates

3.1 The Quasi-State Space Equations of the CCST

This work considers the 3D microstructure-dependent static flexural problem of a simply-supported FG microplate under either a sinusoidally distributed load or a uniform load, and the former loading case is shown in Fig. 3. The symbols h, L_x, and L_y represent the microplate's height, length, and width, respectively. A Cartesian coordinate system (x, y and z) is oriented so that the xy-plane is the microplate's mid-plane.
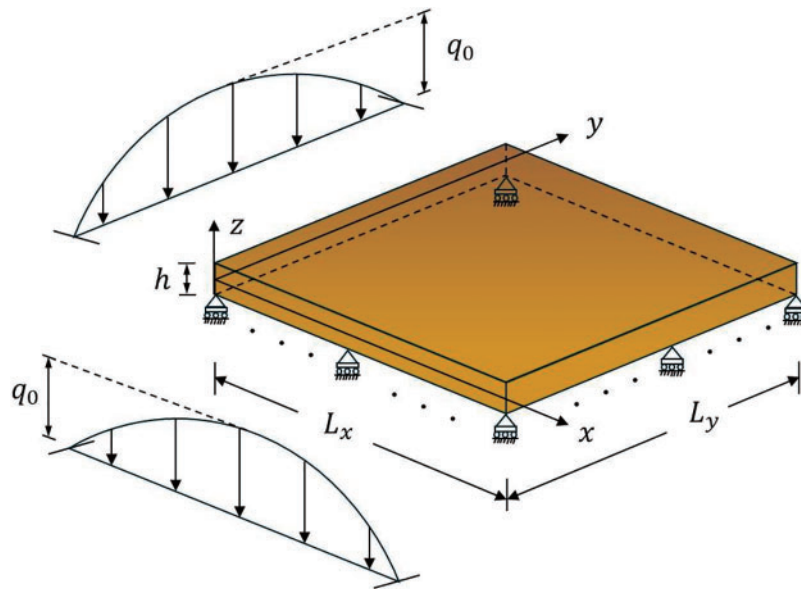
Figure 3: An FG microplate of interest that is subjected to a sinusoidally distributed load

The displacement vector **u** of the deformed microplate is expressed as $\mathbf{u} = u_x\,\mathbf{i} + u_y\,\mathbf{j} + u_z\,\mathbf{k}$, where **i**, **j**, and **k** represent the unit basis vectors in the x, y, and z directions, respectively.

The strain tensor $\boldsymbol{\varepsilon}$ is symmetric, and its relationships with the displacement tensor in Cartesian coordinates are expressed as

$$\varepsilon_{xx} = u_{x,x}, \tag{28a}$$

$$\varepsilon_{yy} = u_{y,y}, \tag{28b}$$

$$\varepsilon_{zz} = u_{z,z}, \tag{28c}$$

$$\gamma_{xz} = 2\varepsilon_{xz} = u_{x,z} + u_{z,x}, \tag{28d}$$

$$\gamma_{yz} = 2\varepsilon_{yz} = u_{y,z} + u_{z,y}, \tag{28e}$$

$$\gamma_{xy} = 2\varepsilon_{xy} = u_{x,y} + u_{y,x}, \tag{28f}$$

where the commas represent the partial derivative of the suffix variable.

The rotation tensor θ is skew-symmetric, and its relationship with the displacement tensor in Cartesian coordinates is expressed as follows:

$$\theta_x = \theta_{zy} = (1/2)\left(u_{z,y} - u_{y,z}\right), \tag{29a}$$

$$\theta_y = \theta_{xz} = (1/2)\left(u_{x,z} - u_{z,x}\right), \tag{29b}$$

$$\theta_z = \theta_{yx} = (1/2)\left(u_{y,x} - u_{x,y}\right). \tag{29c}$$

The symmetric part of the curvature tensor χ-the rotation tensor θ relationship in Cartesian coordinates is expressed as follows:

$$\chi_{xx} = \theta_{x,x}, \tag{30a}$$

$$\chi_{yy} = \theta_{y,y}, \tag{30b}$$

$$\chi_{zz} = \theta_{z,z}, \tag{30c}$$

$$\chi_{xz} = (1/2)\left(\theta_{x,z} + \theta_{z,x}\right), \tag{30d}$$

$$\chi_{yz} = (1/2)\left(\theta_{y,z} + \theta_{z,y}\right), \tag{30e}$$

$$\chi_{xy} = (1/2)\left(\theta_{x,y} + \theta_{y,x}\right). \tag{30f}$$

The skew-symmetric part of the curvature tensor κ-the rotation tensor θ relationship in Cartesian coordinates is expressed as follows:

$$\kappa_x = \kappa_{zy} = (1/2)\left(\theta_{z,y} - \theta_{y,z}\right), \tag{31a}$$

$$\kappa_y = \kappa_{xz} = (1/2)\left(\theta_{x,z} - \theta_{z,x}\right), \tag{31b}$$

$$\kappa_z = \kappa_{yx} = (1/2)\left(\theta_{y,x} - \theta_{x,y}\right). \tag{31c}$$

Hadjesfandiari and Dargush [16,17] indicated that in general, the force-stress tensor (σ_{ij}) induced in the loaded microplate is asymmetric. Therefore, they separated it into a skew-symmetric part ($\sigma_{[ij]}$) and a symmetric ($\sigma_{(ij)}$) part, and represented these two parts using brackets and parentheses that surround a pair of indices, respectively. Subsequently, Hadjesfandiari et al. employed the principle of virtual displacements to deduce a result that the couple-stress tensor μ is skew-symmetric, such that $\mu_x = \mu_{zy} = -\mu_{yz}$, $\mu_y = \mu_{xz} = -\mu_{zx}$, and $\mu_z = \mu_{yx} = -\mu_{xy}$. In addition, they also deduced the force-stress tensor's skew-symmetric part-the couple stress tensor relationship as follows:

$$\sigma_{[ji]} = -\mu_{[i,j]} = -(1/2)\left(\mu_{i,j} - \mu_{j,i}\right). \tag{32}$$

The linear constitutive equations for a loaded orthotropic material microplate are given by

$$
\begin{Bmatrix} \sigma_{(xx)} \\ \sigma_{(yy)} \\ \sigma_{(zz)} \\ \sigma_{(yz)} \\ \sigma_{(xz)} \\ \sigma_{(xy)} \end{Bmatrix} = \begin{bmatrix} c_{11} & c_{12} & c_{13} & 0 & 0 & 0 \\ c_{12} & c_{22} & c_{23} & 0 & 0 & 0 \\ c_{13} & c_{23} & c_{33} & 0 & 0 & 0 \\ 0 & 0 & 0 & c_{44} & 0 & 0 \\ 0 & 0 & 0 & 0 & c_{55} & 0 \\ 0 & 0 & 0 & 0 & 0 & c_{66} \end{bmatrix} \begin{Bmatrix} \varepsilon_{xx} \\ \varepsilon_{yy} \\ \varepsilon_{zz} \\ \gamma_{yz} \\ \gamma_{xz} \\ \gamma_{xy} \end{Bmatrix}, \tag{33}
$$

$$
\begin{Bmatrix} \mu_x \\ \mu_y \\ \mu_z \end{Bmatrix} = \left(-8l^2\right) \begin{bmatrix} G_{32} & 0 & 0 \\ 0 & G_{13} & 0 \\ 0 & 0 & G_{21} \end{bmatrix} \begin{Bmatrix} \kappa_x \\ \kappa_y \\ \kappa_z \end{Bmatrix}, \tag{34}
$$

where c_{ij} $(i,j = 1\text{–}6)$ are the elastic coefficients; and G_{32}, G_{13}, and G_{21} are the shear modulus associated with the zy-, xz-, and yx-planes, respectively. The symbol l represents the microplate's material length-scale parameter, the determination of which refers to Tang et al. [48] and Song et al. [49].

The stress equilibrium equations of a microplate, following Hadjesfandiari and Dargush's analysis [16,17], are given by

$$
\sigma_{(xx),x} + \sigma_{(yx),y} + \sigma_{zx,z} + \sigma_{[yx],y} = 0, \tag{35}
$$

$$
\sigma_{(xy),x} + \sigma_{(yy),y} + \sigma_{zy,z} + \sigma_{[xy],x} = 0, \tag{36}
$$

$$
\sigma_{xz,x} + \sigma_{yz,y} + \sigma_{zz,z} = 0, \tag{37}
$$

where as mentioned above, $\sigma_{ij} = \sigma_{(ij)} + \sigma_{[ij]}$ and $\sigma_{[ij]} = -\sigma_{[ji]}$ for $i \neq j$, and $\sigma_{kk} = \sigma_{(kk)}$.

We employ the direct elimination to reduce the above equations to six partial differential equations which are expressed in terms of six primary variables: three transverse stresses (σ_{zx}, σ_{zy}, and σ_{zz}) and three displacements (u_x, u_y, and u_z).

Substituting Eqs. (32) and (34) into the fifth equation of Eq. (33) leads to

$$
u_{x,z} = - u_{z,x} + c_{55}^{-1}\sigma_{zx} + l^2 \left(G_{21}/c_{55}\right) \left(u_{x,xxz} + u_{y,xyz} - u_{z,xxx} - u_{z,xyy}\right)
$$
$$
\quad + l^2 \left(G_{32}/c_{55}\right) \left(u_{x,yyz} + u_{x,zzz} - u_{y,xyz} - u_{z,xzz}\right) + l^2 \left(G_{32,z}/c_{55}\right) \left(u_{x,yy} + u_{x,zz} - u_{y,xy} - u_{z,xz}\right). \tag{38}
$$

Substituting Eqs. (32) and (34) into the fourth equation of Eq. (33) leads to

$$
u_{y,z} = - u_{z,y} + c_{44}^{-1}\sigma_{zy} + l^2 \left(G_{21}/c_{44}\right) \left(u_{x,xyz} + u_{y,yyz} - u_{z,xxy} - u_{z,yyy}\right)
$$
$$
\quad + l^2 \left(G_{13}/c_{44}\right) \left(-u_{x,xyz} + u_{y,xxz} + u_{y,zzz} - u_{z,yzz}\right) + l^2 \left(G_{13,z}/c_{44}\right) \left(-u_{x,xy} + u_{y,xx} + u_{y,zz} - u_{z,yz}\right). \tag{39}
$$

Substituting Eq. (28c) into the third equation of Eq. (33) leads to

$$
u_{z,z} = -\tilde{c}_{13} u_{x,x} - \tilde{c}_{23} u_{y,y} + c_{33}^{-1}\sigma_{(zz)}, \tag{40}
$$

where $\tilde{c}_{k3} = c_{k3}/c_{33}$ ($k = 1$ and 2).

Using the relationships of $\sigma_{xz} = \sigma_{zx} + 2\sigma_{[xz]}$ and $\sigma_{yz} = \sigma_{zy} + 2\sigma_{[yz]}$ and Eqs. (29), (31), and (32), we can rewrite Eqs. (35)–(37) as follows:

$$\sigma_{zx,z} = -\sigma_{(xx),x} - \sigma_{(yx),y} - (1/2)\,\mu_{y,xy} - (1/2)\,\mu_{x,yy}$$

$$= -Q_{11}u_{x,xx} - Q_{12}u_{y,xy} - \tilde{c}_{13}\sigma_{zz,x} - c_{66}u_{x,yy} - c_{66}u_{y,xy}$$

$$+ l^2 G_{13}\left[u_{x,xxyy} - u_{y,xxxy} - u_{y,xyzz} + u_{z,xyyz}\right] + l^2 G_{32}\left[u_{x,yyyy} + u_{x,yyzz} - u_{y,xyyy} - u_{z,xyyz}\right], \tag{41}$$

$$\sigma_{zy,z} = -\sigma_{(xy),x} - \sigma_{(yy),y} - (1/2)\,\mu_{x,xy} - (1/2)\,\mu_{y,xx}$$

$$= -Q_{12}u_{x,xy} - Q_{22}u_{y,yy} - \tilde{c}_{23}\sigma_{zz,y} - c_{66}u_{x,xy} - c_{66}u_{y,xx}$$

$$+ l^2 G_{32}\left[-u_{x,xyyy} - u_{x,xyzz} + u_{y,xxyy} + u_{z,xxyz}\right] + l^2 G_{13}\left[-u_{x,xxxy} + u_{y,xxxx} + u_{y,xxzz} - u_{z,xxyz}\right], \tag{42}$$

$$\sigma_{zz,z} = -\sigma_{zx,x} - \sigma_{zy,y} - \mu_{x,xz} + \mu_{z,xx} - \mu_{y,yz} + \mu_{z,yy}$$

$$= -\sigma_{zx,x} - \sigma_{zy,y} + 2l^2 G_{32}\left[-u_{x,xyyz} - u_{x,xzzz} + u_{y,xxyz} + u_{z,xxzz}\right] + 2l^2 G_{13}\left[u_{x,xyyz} - u_{y,xxyz} - u_{y,yzzz} + u_{z,yyzz}\right]$$

$$+ 2l^2 G_{21}\left[-u_{x,xxxz} - u_{x,xyyz} - u_{y,xxyz} - u_{y,yyyz} + u_{z,xxxx} + 2u_{z,xxyy} + u_{z,yyyy}\right]$$

$$+ 2l^2 G_{32,z}\left[-u_{x,xyy} - u_{x,xzz} + u_{y,xxy} + u_{z,xxz}\right] + 2l^2 G_{13,z}\left[u_{x,xyy} - u_{y,xxy} - u_{y,yzz} + u_{z,yyz}\right], \tag{43}$$

where $Q_{ij} = c_{ij} - (c_{i3}c_{j3}/c_{33})$ $(i,\ j = 1\ \text{and}\ 2)$.

Eqs. (38)–(43) represent the quasi-state space equations for the FG microplates' 3D microstructure-dependent static flexural behavior. In addition, we can reduce these equations for examining FG microscale plates to those for examining FG macroscale plates by letting the value of l zero.

The microplate's surface and edge boundary conditions are specified in the following forms [16,17]:

On the top and bottom surfaces,

$$\left\{\sigma_{zx}\quad \sigma_{zy}\quad \sigma_{zz}\quad \mu_x\quad \mu_y\right\} = \left\{0\quad 0\quad \bar{q}_z^{\pm}\quad 0\quad 0\right\} \qquad \text{on} \qquad z = \pm h/2, \tag{44}$$

where the positive directions of $\bar{q}_z^-$ and $\bar{q}_z^+$, following the conventions of the 3D elasticity theory, are defined to be downward and upward, respectively.

For simply supported boundary edges, we express the edge boundary conditions in the following forms:

At the edges $x = 0$ and $x = L_x$,

$$\sigma_{xx} = u_y = u_z = \mu_y = \mu_z = 0. \tag{45a}$$

At the edges $y = 0$ and $y = L_y$,

$$\sigma_{yy} = u_x = u_z = \mu_x = \mu_z = 0. \tag{45b}$$

3.2 Fourier Series Expansion Method

This work lets the external loads $\bar{q}_z^-(x,y) = 0$ and expands $\bar{q}_z^+(x,y)$ as a double Fourier series as follows:

$$\bar{q}_z^+(x,y) = \sum_{\hat{m}=1}^{\infty}\sum_{\hat{n}=1}^{\infty} q_{\hat{m}\hat{n}}\sin\tilde{m}x\ \sin\tilde{n}y, \tag{46}$$

where the symbols $\tilde{m} = \hat{m}\pi/L_x$ and $\tilde{n} = \hat{n}\pi/L_y$; and the symbols $\hat{m}$ and $\hat{n}$ are the half-wave numbers.

We also express these primary variables as the following double Fourier series:

$$u_x(x, y, z) = \sum_{\hat{m}=1}^{\infty} \sum_{\hat{n}=1}^{\infty} u_{\hat{m}\hat{n}}(z) \cos \tilde{m}x \sin \tilde{n}y, \tag{47}$$

$$u_y(x, y, z) = \sum_{\hat{m}=1}^{\infty} \sum_{\hat{n}=1}^{\infty} v_{\hat{m}\hat{n}}(z) \sin \tilde{m}x \cos \tilde{n}y, \tag{48}$$

$$u_z(x, y, z) = \sum_{\hat{m}=1}^{\infty} \sum_{\hat{n}=1}^{\infty} w_{\hat{m}\hat{n}}(z) \sin \tilde{m}x \sin \tilde{n}y, \tag{49}$$

$$\sigma_{zx}(x, y, z) = \sum_{\hat{m}=1}^{\infty} \sum_{\hat{n}=1}^{\infty} \sigma_{31\hat{m}\hat{n}}(z) \cos \tilde{m}x \sin \tilde{n}y, \tag{50}$$

$$\sigma_{zy}(x, y, z) = \sum_{\hat{m}=1}^{\infty} \sum_{\hat{n}=1}^{\infty} \sigma_{32\hat{m}\hat{n}}(z) \sin \tilde{m}x \cos \tilde{n}y, \tag{51}$$

$$\sigma_{zz}(x, y, z) = \sum_{\hat{m}=1}^{\infty} \sum_{\hat{n}=1}^{\infty} \sigma_{33\hat{m}\hat{n}}(z) \sin \tilde{m}x \sin \tilde{n}y. \tag{52}$$

Substituting Eqs. (47)–(52) into the quasi-state space Eqs. (38)–(43) yields

$$
\begin{aligned}
u_{\hat{m}\hat{n},z} = &-\tilde{m}w_{\hat{m}\hat{n}} + c_{55}^{-1}\sigma_{31\hat{m}\hat{n}} + l^2\left(G_{21}/c_{55}\right)\left(-\tilde{m}^2 u_{\hat{m}\hat{n},z} - \tilde{m}\tilde{n}v_{\hat{m}\hat{n},z} + \tilde{m}^3 w_{\hat{m}\hat{n}} + \tilde{m}\tilde{n}^2 w_{\hat{m}\hat{n}}\right) \\
&+ l^2\left(G_{32}/c_{55}\right)\left(-\tilde{n}^2 u_{\hat{m}\hat{n},z} + u_{\hat{m}\hat{n},zzz} + \tilde{m}\tilde{n}v_{\hat{m}\hat{n},z} - \tilde{m}w_{\hat{m}\hat{n},zz}\right) \\
&+ l^2\left(G_{32,z}/c_{55}\right)\left(-\tilde{n}^2 u_{\hat{m}\hat{n}} + u_{\hat{m}\hat{n},zz} + \tilde{m}\tilde{n}v_{\hat{m}\hat{n}} - \tilde{m}w_{\hat{m}\hat{n},z}\right),
\end{aligned} \tag{53}
$$

$$
\begin{aligned}
v_{\hat{m}\hat{n},z} = &-\tilde{n}w_{\hat{m}\hat{n}} + c_{44}^{-1}\sigma_{32\hat{m}\hat{n}} + l^2\left(G_{21}/c_{44}\right)\left[-\tilde{m}\tilde{n}u_{\hat{m}\hat{n},z} - \tilde{n}^2 v_{\hat{m}\hat{n},z} + \left(\tilde{m}^2\tilde{n} + \tilde{n}^3\right)w_{\hat{m}\hat{n}}\right] \\
&+ l^2\left(G_{13}/c_{44}\right)\left(\tilde{m}\tilde{n}u_{\hat{m}\hat{n},z} - \tilde{m}^2 v_{\hat{m}\hat{n},z} + v_{\hat{m}\hat{n},zzz} - \tilde{n}w_{\hat{m}\hat{n},zz}\right) \\
&+ l^2\left(G_{13,z}/c_{44}\right)\left(\tilde{m}\tilde{n}u_{\hat{m}\hat{n}} - \tilde{m}^2 v_{\hat{m}\hat{n}} + v_{\hat{m}\hat{n},zz} - \tilde{n}w_{\hat{m}\hat{n},z}\right),
\end{aligned} \tag{54}
$$

$$w_{\hat{m}\hat{n},z} = \tilde{m}\tilde{c}_{13}u_{\hat{m}\hat{n}} + \tilde{n}\tilde{c}_{23}v_{\hat{m}\hat{n}} + c_{33}^{-1}\sigma_{33\hat{m}\hat{n}}, \tag{55}$$

$$
\begin{aligned}
\sigma_{31\hat{m}\hat{n},z} = &\tilde{m}^2 Q_{11}u_{\hat{m}\hat{n}} + \tilde{m}\tilde{n}Q_{12}v_{\hat{m}\hat{n}} - \tilde{m}\tilde{c}_{13}\sigma_{33\hat{m}\hat{n}} + \tilde{n}^2 c_{66}u_{\hat{m}\hat{n}} + \tilde{m}\tilde{n}c_{66}v_{\hat{m}\hat{n}} \\
&+ l^2 G_{13}\left(\tilde{m}^2\tilde{n}^2 u_{\hat{m}\hat{n}} - \tilde{m}^3\tilde{n}v_{\hat{m}\hat{n}} + \tilde{m}\tilde{n}v_{\hat{m}\hat{n},zz} - \tilde{m}\tilde{n}^2 w_{\hat{m}\hat{n},z}\right) \\
&+ l^2 G_{32}\left(\tilde{n}^4 u_{\hat{m}\hat{n}} - \tilde{n}^2 u_{\hat{m}\hat{n},zz} - \tilde{m}\tilde{n}^3 v_{\hat{m}\hat{n}} + \tilde{m}\tilde{n}^2 w_{\hat{m}\hat{n},z}\right),
\end{aligned} \tag{56}
$$

$$
\begin{aligned}
\sigma_{32\hat{m}\hat{n},z} = &\tilde{m}\tilde{n}Q_{12}u_{\hat{m}\hat{n}} + \tilde{n}^2 Q_{22}v_{\hat{m}\hat{n}} - \tilde{n}\tilde{c}_{23}\sigma_{33\hat{m}\hat{n}} + \tilde{m}\tilde{n}c_{66}u_{\hat{m}\hat{n}} + \tilde{m}^2 c_{66}v_{\hat{m}\hat{n}} \\
&+ l^2 G_{32}\left[-\tilde{m}\tilde{n}^3 u_{\hat{m}\hat{n}} + \tilde{m}\tilde{n}u_{\hat{m}\hat{n},zz} + \tilde{m}^2\tilde{n}^2 v_{\hat{m}\hat{n}} - \tilde{m}^2\tilde{n}w_{\hat{m}\hat{n},z}\right] \\
&+ l^2 G_{13}\left[-\tilde{m}^3\tilde{n}u_{\hat{m}\hat{n}} + \tilde{m}^4 v_{\hat{m}\hat{n}} - \tilde{m}^2 v_{\hat{m}\hat{n},zz} + \tilde{m}^2\tilde{n}w_{\hat{m}\hat{n},z}\right],
\end{aligned} \tag{57}
$$

$$\sigma_{33\hat{m}\hat{n},z} = \tilde{m}\sigma_{31\hat{m}\hat{n}} + \tilde{n}\sigma_{32\hat{m}\hat{n}} + 2l^2 G_{32}\left(-\tilde{m}\tilde{n}^2 u_{\hat{m}\hat{n},z} + \tilde{m}u_{\hat{m}\hat{n},zzz} + \tilde{m}^2\tilde{n}v_{\hat{m}\hat{n},z} - \tilde{m}^2 w_{\hat{m}\hat{n},zz}\right)$$

$$+ 2l^2 G_{13}\left(\tilde{m}\tilde{n}^2 u_{\hat{m}\hat{n},z} - \tilde{m}^2\tilde{n}v_{\hat{m}\hat{n},z} + \tilde{n}v_{\hat{m}\hat{n},zzz} - \tilde{n}^2 w_{\hat{m}\hat{n},zz}\right)$$

$$+ 2l^2 G_{21}\left[-\left(\tilde{m}^3 + \tilde{m}\tilde{n}^2\right)u_{\hat{m}\hat{n},z} - \left(\tilde{m}^2\tilde{n} + \tilde{n}^3\right)v_{\hat{m}\hat{n},z} + \left(\tilde{m}^4 + 2\tilde{m}^2\tilde{n}^2 + \tilde{n}^4\right)w_{\hat{m}\hat{n}}\right]$$

$$+ 2l^2 G_{32,z}\left(-\tilde{m}\tilde{n}^2 u_{\hat{m}\hat{n}} + \tilde{m}u_{\hat{m}\hat{n},zz} + \tilde{m}^2\tilde{n}v_{\hat{m}\hat{n}} - \tilde{m}^2 w_{\hat{m}\hat{n},z}\right)$$

$$+ 2l^2 G_{13,z}\left(\tilde{m}\tilde{n}^2 u_{\hat{m}\hat{n}} - \tilde{m}^2\tilde{n}v_{\hat{m}\hat{n}} + \tilde{n}v_{\hat{m}\hat{n},zz} - \tilde{n}^2 w_{\hat{m}\hat{n},z}\right). \tag{58}$$

3.3 The Hermitian C^2 DRKIM Method

This section develops the Hermitian C^2 DRKIM method, which is a point collocation, for solving the strong form of the 3D CCST, which is composed of the quasi-state space Eqs. (53)–(58) and their associated boundary conditions (45a) and (45b).

First, we select n_c collocation points in the thickness direction, for which $n_c = 3n_p$, and then substitute the primary variables expressed in Eq. (1) and their relevant derivatives into the quasi-state space Eqs. (53)–(58) at the ith-collocation point, which leads to the following algebraic equations:

$$\sum_{j=1}^{np}\left\{\left[\left(\tilde{d}_{11}N_{ij}^{(3)} + \tilde{d}_{12}N_{ij}^{(2)} + \tilde{d}_{13}N_{ij}^{(1)} + \tilde{d}_{14}N_{ij}\right)(u_{\hat{m}\hat{n}})_j + \left(\tilde{d}_{11}\hat{N}_{ij}^{(3)} + \tilde{d}_{12}\hat{N}_{ij}^{(2)} + \tilde{d}_{13}\hat{N}_{ij}^{(1)} + \tilde{d}_{14}\hat{N}_{ij}\right)(\theta_{u\hat{m}\hat{n}})_j\right.\right.$$

$$+ \left(\tilde{d}_{11}\overline{N}_{ij}^{(3)} + \tilde{d}_{12}\overline{N}_{ij}^{(2)} + \tilde{d}_{13}\overline{N}_{ij}^{(1)} + \tilde{d}_{14}\overline{N}_{ij}\right)(\kappa_{u\hat{m}\hat{n}})_j\right] + \left[\left(\tilde{d}_{15}N_{ij}^{(1)} + \tilde{d}_{16}N_{ij}\right)(v_{\hat{m}\hat{n}})_j + \left(\tilde{d}_{15}\hat{N}_{ij}^{(1)} + \tilde{d}_{16}\hat{N}_{ij}\right)(\theta_{v\hat{m}\hat{n}})_j$$

$$+ \left(\tilde{d}_{15}\overline{N}_{ij}^{(1)} + \tilde{d}_{16}\overline{N}_{ij}\right)(\kappa_{v\hat{m}\hat{n}})_j\right] + \left[\left(\tilde{d}_{17}N_{ij}^{(2)} + \tilde{d}_{18}N_{ij}^{(1)} + \tilde{d}_{19}N_{ij}\right)(w_{\hat{m}\hat{n}})_j + \left(\tilde{d}_{17}\hat{N}_{ij}^{(2)} + \tilde{d}_{18}\hat{N}_{ij}^{(1)} + \tilde{d}_{19}\hat{N}_{ij}\right)(\theta_{w\hat{m}\hat{n}})_j$$

$$+ \left(\tilde{d}_{17}\overline{N}_{ij}^{(2)} + \tilde{d}_{18}\overline{N}_{ij}^{(1)} + \tilde{d}_{19}\overline{N}_{ij}\right)(\kappa_{w\hat{m}\hat{n}})_j\right] + \left[\tilde{d}_{110}N_{ij}(\sigma_{31\hat{m}\hat{n}})_j + \tilde{d}_{110}\hat{N}_{ij}(\theta_{\sigma31\hat{m}\hat{n}})_j + \tilde{d}_{110}\overline{N}_{ij}(\kappa_{\sigma31\hat{m}\hat{n}})_j\right]\right\} = 0, \tag{59}$$

$$\sum_{j=1}^{np}\left\{\left[\left(\tilde{d}_{21}N_{ij}^{(1)} + \tilde{d}_{22}N_{ij}\right)(u_{\hat{m}\hat{n}})_j + \left(\tilde{d}_{21}\hat{N}_{ij}^{(1)} + \tilde{d}_{22}\hat{N}_{ij}\right)(\theta_{u\hat{m}\hat{n}})_j + \left(\tilde{d}_{21}\overline{N}_{ij}^{(1)} + \tilde{d}_{22}\overline{N}_{ij}\right)(\kappa_{u\hat{m}\hat{n}})_j\right]\right.$$

$$+ \left[\left(\tilde{d}_{23}N_{ij}^{(3)} + \tilde{d}_{24}N_{ij}^{(2)} + \tilde{d}_{25}N_{ij}^{(1)} + \tilde{d}_{26}N_{ij}\right)(v_{\hat{m}\hat{n}})_j + \left(\tilde{d}_{23}\hat{N}_{ij}^{(3)} + \tilde{d}_{24}\hat{N}_{ij}^{(2)} + \tilde{d}_{25}\hat{N}_{ij}^{(1)} + \tilde{d}_{26}\hat{N}_{ij}\right)(\theta_{v\hat{m}\hat{n}})_j$$

$$+ \left(\tilde{d}_{23}\overline{N}_{ij}^{(3)} + \tilde{d}_{24}\overline{N}_{ij}^{(2)} + \tilde{d}_{25}\overline{N}_{ij}^{(1)} + \tilde{d}_{26}\overline{N}_{ij}\right)(\kappa_{v\hat{m}\hat{n}})_j\right] + \left[\left(\tilde{d}_{27}N_{ij}^{(2)} + \tilde{d}_{28}N_{ij}^{(1)} + \tilde{d}_{29}N_{ij}\right)(w_{\hat{m}\hat{n}})_j$$

$$+ \left(\tilde{d}_{27}\hat{N}_{ij}^{(2)} + \tilde{d}_{28}\hat{N}_{ij}^{(1)} + \tilde{d}_{29}\hat{N}_{ij}\right)(\theta_{w\hat{m}\hat{n}})_j + + \left(\tilde{d}_{27}\overline{N}_{ij}^{(2)} + \tilde{d}_{28}\overline{N}_{ij}^{(1)} + \tilde{d}_{29}\overline{N}_{ij}\right)(\kappa_{w\hat{m}\hat{n}})_j\right]$$

$$+ \left[\tilde{d}_{210}N_{ij}(\sigma_{32\hat{m}\hat{n}})_j + \tilde{d}_{210}\hat{N}_{ij}(\theta_{\sigma32\hat{m}\hat{n}})_j + \tilde{d}_{210}\overline{N}_{ij}(\kappa_{\sigma32\hat{m}\hat{n}})\right]\right\} = 0, \tag{60}$$

$$\sum_{j=1}^{np}\left\{\left[\tilde{d}_{31}N_{ij}(u_{\hat{m}\hat{n}})_j + \tilde{d}_{31}\hat{N}_{ij}(\theta_{u\hat{m}\hat{n}})_j + \tilde{d}_{31}\overline{N}_{ij}(\kappa_{u\hat{m}\hat{n}})_j\right] + \left[\tilde{d}_{32}N_{ij}(v_{\hat{m}\hat{n}})_j + \tilde{d}_{32}\hat{N}_{ij}(\theta_{v\hat{m}\hat{n}})_j + \tilde{d}_{32}\overline{N}_{ij}(\kappa_{v\hat{m}\hat{n}})_j\right]\right.$$

$$- \left[N_{ij}^{(1)}(w_{\hat{m}\hat{n}})_j + \hat{N}_{ij}^{(1)}(\theta_{w\hat{m}\hat{n}})_j + \overline{N}_{ij}^{(1)}(\kappa_{w\hat{m}\hat{n}})_j\right] + \left[\tilde{d}_{33}N_{ij}(\sigma_{33\hat{m}\hat{n}})_j + \tilde{d}_{33}\hat{N}_{ij}(\theta_{\sigma33\hat{m}\hat{n}})_j + \tilde{d}_{33}\overline{N}_{ij}(\kappa_{\sigma33\hat{m}\hat{n}})_j\right]\right\} = 0, \tag{61}$$

$$\sum_{j=1}^{np} \left\{ \left[\left(\tilde{d}_{41} N_{ij}^{(2)} + \tilde{d}_{42} N_{ij} \right) (u_{\hat{m}\hat{n}})_j + \left(\tilde{d}_{41} \hat{N}_{ij}^{(2)} + \tilde{d}_{42} \hat{N}_{ij} \right) (\theta_{u\hat{m}\hat{n}})_j + \left(\tilde{d}_{41} \overline{N}_{ij}^{(2)} + \tilde{d}_{42} \overline{N}_{ij} \right) (\kappa_{u\hat{m}\hat{n}})_j \right] \right.$$

$$+ \left[\left(\tilde{d}_{43} N_{ij}^{(2)} + \tilde{d}_{44} N_{ij} \right) (v_{\hat{m}\hat{n}})_j + \left(\tilde{d}_{43} \hat{N}_{ij}^{(2)} + \tilde{d}_{44} \hat{N}_{ij} \right) (\theta_{v\hat{m}\hat{n}})_j + \left(\tilde{d}_{43} \overline{N}_{ij}^{(2)} + \tilde{d}_{44} \overline{N}_{ij} \right) (\kappa_{v\hat{m}\hat{n}})_j \right]$$

$$+ \left[\tilde{d}_{45} N_{ij}^{(1)} (w_{\hat{m}\hat{n}})_j + \tilde{d}_{45} \hat{N}_{ij}^{(1)} (\theta_{w\hat{m}\hat{n}})_j + \tilde{d}_{45} \overline{N}_{ij}^{(1)} (\kappa_{w\hat{m}\hat{n}})_j \right] - \left[N_{ij}^{(1)} (\sigma_{31\hat{m}\hat{n}})_j + \hat{N}_{ij}^{(1)} (\theta_{\sigma 31\hat{m}\hat{n}})_j + \overline{N}_{ij}^{(1)} (\kappa_{\sigma 31\hat{m}\hat{n}})_j \right]$$

$$\left. + \left[\tilde{d}_{46} N_{ij} (\sigma_{33\hat{m}\hat{n}})_j + \tilde{d}_{46} \hat{N}_{ij} (\theta_{\sigma 33\hat{m}\hat{n}})_j + \tilde{d}_{46} \overline{N}_{ij} (\kappa_{\sigma 33\hat{m}\hat{n}})_j \right] \right\} = 0, \tag{62}$$

$$\sum_{j=1}^{np} \left\{ \left[\left(\tilde{d}_{51} N_{ij}^{(2)} + \tilde{d}_{52} N_{ij} \right) (u_{\hat{m}\hat{n}})_j + \left(\tilde{d}_{51} \hat{N}_{ij}^{(2)} + \tilde{d}_{52} \hat{N}_{ij} \right) (\theta_{u\hat{m}\hat{n}})_j + \left(\tilde{d}_{51} \overline{N}_{ij}^{(2)} + \tilde{d}_{52} \overline{N}_{ij} \right) (\kappa_{u\hat{m}\hat{n}})_j \right] \right.$$

$$+ \left[\left(\tilde{d}_{53} N_{ij}^{(2)} + \tilde{d}_{54} N_{ij} \right) (v_{\hat{m}\hat{n}})_j + \left(\tilde{d}_{53} \hat{N}_{ij}^{(2)} + \tilde{d}_{54} \hat{N}_{ij} \right) (\theta_{v\hat{m}\hat{n}})_j + \left(\tilde{d}_{53} \overline{N}_{ij}^{(2)} + \tilde{d}_{54} \overline{N}_{ij} \right) (\kappa_{v\hat{m}\hat{n}})_j \right]$$

$$+ \left[\tilde{d}_{55} N_{ij}^{(1)} (w_{\hat{m}\hat{n}})_j + \tilde{d}_{55} \hat{N}_{ij}^{(1)} (\theta_{w\hat{m}\hat{n}})_j + \tilde{d}_{55} \overline{N}_{ij}^{(1)} (\kappa_{w\hat{m}\hat{n}})_j \right] - \left[N_{ij}^{(1)} (\sigma_{32\hat{m}\hat{n}})_j + \hat{N}_{ij}^{(1)} (\theta_{\sigma 32\hat{m}\hat{n}})_j + \overline{N}_{ij}^{(1)} (\kappa_{\sigma 32\hat{m}\hat{n}})_j \right]$$

$$\left. + \left[\tilde{d}_{56} N_{ij} (\sigma_{33\hat{m}\hat{n}})_j + \tilde{d}_{56} \hat{N}_{ij} (\theta_{\sigma 33\hat{m}\hat{n}})_j + \tilde{d}_{56} \overline{N}_{ij} (\kappa_{\sigma 33\hat{m}\hat{n}})_j \right] \right\} = 0, \tag{63}$$

$$\sum_{j=1}^{np} \left\{ \left[\left(\tilde{d}_{61} N_{ij}^{(3)} + \tilde{d}_{62} N_{ij}^{(2)} + \tilde{d}_{63} N_{ij}^{(1)} + \tilde{d}_{64} N_{ij} \right) (u_{\hat{m}\hat{n}})_j + \left(\tilde{d}_{61} \hat{N}_{ij}^{(3)} + \tilde{d}_{62} \hat{N}_{ij}^{(2)} + \tilde{d}_{63} \hat{N}_{ij}^{(1)} + \tilde{d}_{64} \hat{N}_{ij} \right) (\theta_{u\hat{m}\hat{n}})_j \right. \right.$$

$$+ \left(\tilde{d}_{61} \overline{N}_{ij}^{(3)} + \tilde{d}_{62} \overline{N}_{ij}^{(2)} + \tilde{d}_{63} \overline{N}_{ij}^{(1)} + \tilde{d}_{64} \overline{N}_{ij} \right) (\kappa_{u\hat{m}\hat{n}})_j \right] + \left[\left(\tilde{d}_{65} N_{ij}^{(3)} + \tilde{d}_{66} N_{ij}^{(2)} + \tilde{d}_{67} N_{ij}^{(1)} + \tilde{d}_{68} N_{ij} \right) (v_{\hat{m}\hat{n}})_j \right.$$

$$+ \left(\tilde{d}_{65} \hat{N}_{ij}^{(3)} + \tilde{d}_{66} \hat{N}_{ij}^{(2)} + \tilde{d}_{67} \hat{N}_{ij}^{(1)} + \tilde{d}_{68} \hat{N}_{ij} \right) (\theta_{v\hat{m}\hat{n}})_j + \left(\tilde{d}_{65} \overline{N}_{ij}^{(3)} + \tilde{d}_{66} \overline{N}_{ij}^{(2)} + \tilde{d}_{67} \overline{N}_{ij}^{(1)} + \tilde{d}_{68} \overline{N}_{ij} \right) (\kappa_{v\hat{m}\hat{n}})_j \right]$$

$$+ \left[\left(\tilde{d}_{69} N_{ij}^{(2)} + \tilde{d}_{610} N_{ij}^{(1)} + \tilde{d}_{611} N_{ij} \right) (w_{\hat{m}\hat{n}})_j + \left(\tilde{d}_{69} \hat{N}_{ij}^{(2)} + \tilde{d}_{610} \hat{N}_{ij}^{(1)} + \tilde{d}_{611} \hat{N}_{ij} \right) (\theta_{w\hat{m}\hat{n}})_j \right.$$

$$+ \left(\tilde{d}_{69} \overline{N}_{ij}^{(2)} + \tilde{d}_{610} \overline{N}_{ij}^{(1)} + \tilde{d}_{611} \overline{N}_{ij} \right) (\kappa_{w\hat{m}\hat{n}})_j \right] + \left[\tilde{m} N_{ij} (\sigma_{31\hat{m}\hat{n}})_j + \tilde{m} \hat{N}_{ij} (\theta_{\sigma 31\hat{m}\hat{n}})_j + \tilde{m} \overline{N}_{ij} (\kappa_{\sigma 31\hat{m}\hat{n}})_j \right]$$

$$\left. + \left[\tilde{n} N_{ij} (\sigma_{32\hat{m}\hat{n}})_j + \tilde{n} \hat{N}_{ij} (\theta_{\sigma 32\hat{m}\hat{n}})_j + \tilde{n} \overline{N}_{ij} (\kappa_{\sigma 32\hat{m}\hat{n}})_j \right] - \left[N_{ij}^{(1)} (\sigma_{33\hat{m}\hat{n}})_j + \hat{N}_{ij}^{(1)} (\theta_{\sigma 33\hat{m}\hat{n}})_j + \overline{N}_{ij}^{(1)} (\kappa_{\sigma 33\hat{m}\hat{n}})_j \right] \right\} = 0, \tag{64}$$

where $i = 1, 2, \ldots, n_c$; and the relevant coefficients are given in Appendix B.

The associated surface conditions, which are five conditions on the top surface and five conditions on the bottom surface, are given as

$$(\sigma_{31\hat{m}\hat{n}})_1 = (\sigma_{32\hat{m}\hat{n}})_1 = (\sigma_{33\hat{m}\hat{n}})_1 = (\mu_{x\hat{m}\hat{n}})_1 = (\mu_{y\hat{m}\hat{n}})_1 = 0 \qquad \text{when } z = -h/2, \tag{65a}$$

$$(\sigma_{31\hat{m}\hat{n}})_{n_c} = (\sigma_{32\hat{m}\hat{n}})_{n_c} = (\mu_{x\hat{m}\hat{n}})_{n_c} = (\mu_{y\hat{m}\hat{n}})_{n_c} = 0 \text{ and } \quad (\sigma_{33\hat{m}\hat{n}})_{n_c} = \overline{q}_{\hat{m}\hat{n}} \quad \text{when } z = h/2. \tag{65b}$$

As mentioned above, Eqs. (59)–(64) and (65a), (65b) represent a system of $(6n_c + 10)$ (i.e., $18n_p + 10$) algebraic equations in terms of $18n_p$ nodal primary variables, which can be readily solved employing the weighted least square method.

4 Numerical Examples

4.1 Validation and Comparison Studies

This section considers a simply supported FG microplate that is subjected to either a sinusoidally distributed load or a uniform load. The former loading conditions are shown in Fig. 3.

The microplate of interest is made of alumina (Al_2O_3, a ceramic material) and aluminum (Al, a metal material). The microplate's material properties are assumed to obey the power-law distributions for the constituents' volume fractions, which vary in the thickness direction and are defined as follows:

$$\Gamma_{cer}(z) = [(1/2) + (z/h)]^{\kappa_p},$$ (66a)

and

$$\Gamma_{met}(z) = 1 - \Gamma_c(z),$$ (66b)

where the subscripts *cer* and *met* denote the ceramic and metal materials, respectively.

The material properties of the alumina and the aluminum are given in the following form [23]:

For alumina material, $E_{cer} = 380$ GPa, $\upsilon_{cer} = 0.3$, and $\rho_{cer} = 3800$ kg/m³. (67a)

For aluminum material,

$$E_{met} = 70 \text{ GPa}, \quad \upsilon_{met} = 0.3, \quad \text{and } \rho_{met} = 2702 \text{ kg/m}^3.$$ (67b)

By using the rule of mixtures, we estimate the microplate's effective material properties as follows:

$$E_{eff}(z) = E_{cer}\Gamma_{cer}(z) + E_{met}\Gamma_{met}(z)$$
$$= E_{met} + (E_{cer} - E_{met})\,\Gamma_{cer}(z),$$ (68a)

$$\upsilon_{eff}(z) = 0.3.$$ (68b)

For comparison purposes, we define the non-dimensional variables in the same way as those used in Thai et al. [23]:

$$(\overline{u}, \overline{w}) = (u_x, u_\varsigma)\left[10E_{cer}\,h^3/\left(q_0L_x^4\right)\right],$$ (69a)

$$\overline{\sigma}_{ij} = \sigma_{ij}\,h/(q_0L_x) \quad (i, j = x, y, \text{ and } z), \text{ except } \overline{\sigma}_{\varsigma\varsigma} = \sigma_{\varsigma\varsigma}/q_0.$$ (69b)

When considering a homogeneous isotropic microplate, we change E_{cer} in Eq. (69a) to the microplate's Young's modulus, E_0.

According to Lam et al.'s experimental results [7], this work defines the material length-scale parameters of the MCST and the CCST, $\hat{l}$ and l, respectively, as $\hat{l} = 2l = 17.6 \times 10^{-6}$ m. This is because the couple stress tensor (m_{ij})-the curvature tensor (χ_{ij}) relationship in the MCST is $m_{ij} = 2G\hat{l}^2\chi_{ij}$; however, the couple stress tensor (μ_{ij})-the curvature tensor (κ_{ij}) relationship in CCST is $\mu_{ij} = -8G\,l^2\kappa_{ij}$. Thus, the relationship $\hat{l} = 2l$ is obtained, which can be employed to carry out a comprehensive comparison between the solutions obtained using the MCST and the CCST.

Table 1 shows the results of the Hermitian C^2 DRK meshless method for the central deflection (i.e., $\overline{w}(L_x/2, L_y/2, 0)$) of a homogeneous microplate that is placed under full simple supports and is subjected to a sinusoidally distributed load, i.e., $\overline{q}_z^+(x, y) = q_0\sin(\pi x/L_x)\sin(\pi y/L_y)$ and $\overline{q}_z^-(x, y) = 0$. The relevant material parameters are $l/h = 0, 0.1, 0.2, 0.3, 0.4,$ and 0.5. The relevant geometric parameters are $L_x = L_y$ and $L_x/h = 5$. In Table 1, there are three types of sampling node distributions,

which are Types A, B, and C, used with the total number of sampling nodes (n_p) being $n_p = 13$, 17, and 21, and with the base functions' highest order being $n = 4$ and 5. In the case of Type A, the sampling nodes are uniformly distributed. In the case of Type B, distributions of the sampling nodes are selected using a formula of roots of the Chebyshev polynomial, which is $\xi_i = -\cos\left[(i-1)\pi/(n_p - 1)\right]$, where $i = 1, 2, \cdots, n_p$. In the case of Type C, the sampling nodes are randomly scattered and have coordinates that are randomly generated by the computer we used. The sampling node distributions of Types A, B, and C are shown in Table 2.

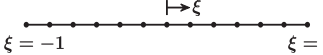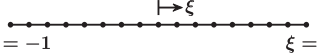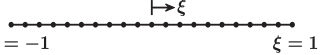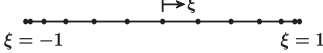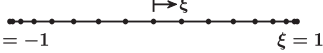**Table 1:** Convergence and accuracy studies for the central deflection of the homogeneous microplate obtained using our Hermitian C^2 DRKIM method with different types of sampling node distributions and different values of the highest order of the base functions

Theories	Sampling node distributions	$\hat{l}/h = 0$ ($l/h = 0$)	$\hat{l}/h = 0.2$ ($l/h = 0.1$)	$\hat{l}/h = 0.4$ ($l/h = 0.2$)	$\hat{l}/h = 0.6$ ($l/h = 0.3$)	$\hat{l}/h = 0.8$ ($l/h = 0.4$)	$\hat{l}/h = 1.0$ ($l/h = 0.5$)
Hermitian C^2 DRK meshless method ($n_p = 13$, $n = 4$)	Type A	0.3367	0.2763	0.1963	0.1332	0.0943	0.0704
	Type B	0.3420	0.2887	0.1909	0.1323	0.0938	0.0700
	Type C	0.3284	0.2606	0.1894	0.1328	0.0942	0.0703
Hermitian C^2 DRK meshless method ($n_p = 17$, $n = 4$)	Type A	0.3366	0.2767	0.1957	0.1339	0.0948	0.0706
	Type B	0.3362	0.2858	0.1962	0.1335	0.0944	0.0704
	Type C	0.3365	0.2777	0.2049	0.1365	0.0929	0.0708
Hermitian C^2 DRK meshless method ($n_p = 21$, $n = 4$)	Type A	0.3365	0.2929	0.1977	0.1345	0.0950	0.0707
	Type B	0.3361	0.2859	0.1993	0.1349	0.0949	0.0706
	Type C	0.3308	0.2990	0.2021	0.1361	0.0944	0.0701
Hermitian C^2 DRK meshless method ($n_p = 13$, $n = 5$)	Type A	0.3363	0.2861	0.1994	0.1351	0.0953	0.0709
	Type B	0.3382	0.2864	0.1994	0.1352	0.0955	0.0710
	Type C	0.3389	0.2758	0.1975	0.1343	0.0951	0.0708
Hermitian C^2 DRK meshless method ($n_p = 17$, $n = 5$)	Type A	0.3353	0.2841	0.1989	0.1351	0.0953	0.0709
	Type B	0.3367	0.2878	0.1995	0.1352	0.0954	0.0709
	Type C	0.3363	0.2864	0.1990	0.1352	0.0954	0.0709
Hermitian C^2 DRK meshless method ($n_p = 21$, $n = 5$)	Type A	0.3361	0.2841	0.1990	0.1350	0.0953	0.0709
	Type B	0.3351	0.2870	0.1994	0.1351	0.0953	0.0709
	Type C	0.3385	0.2911	0.1978	0.1348	0.0954	0.0710
3D MCST [50]		0.3357	0.2851	0.1991	0.1351	0.0953	0.0709
3D CCST-based FEM [51]		0.3357	0.2851	0.1991	0.1351	0.0953	0.0709
MCST-based RSDT [23]		0.3433	0.2875	0.1934	0.1251	0.0838	0.0588

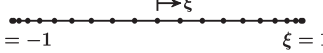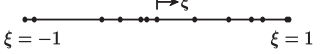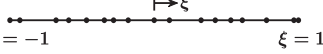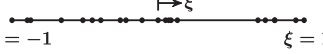Compared with the 3D solutions [50,51], Table 1 shows that the solutions obtained using our Hermitian C^2 DRKIM method with $n = 5$ are more accurate than those with $n = 4$. The solutions obtained using the Hermitian C^2 DRKIM method with the sampling node distributions of Types A and B are more precise than those with Type C sampling node distributions. For a range of the values of the l/h ratio from $l/h = 0$ to $l/h = 0.5$, the maximum relative error between the solutions obtained using the Hermitian C^2 DRKIM method and those obtained using the 3D MCST [50] is 0.35% and 0.67% for Type A and Type B sampling node distributions, respectively. The relative error between the solutions obtained using 3D MCST and the 2D RSDT [23] is 2.3% in the case of $l/h = 0$, and it increases up to 17.1% in the case of $l/h = 0.5$. This is because the 3D couple stress effect is significant

when the value of the l/h ratio increases. Because our Hermitian C^2 DRKIM method is based on the strong form of the 3D CCST, its performance is superior to that of the 2D MCST-based microplate theory, especially for the microplates with a higher value of the l/h ratio.

Table 2: Sampling node distribution of Types A, B, and C

Sampling node distributions	$n_p = 13$	$n_p = 17$	$n_p = 21$
Type A	$\mapsto \xi$ $\xi = -1$ $\xi = 1$	$\mapsto \xi$ $\xi = -1$ $\xi = 1$	$\mapsto \xi$ $\xi = -1$ $\xi = 1$
Type B	$\mapsto \xi$ $\xi = -1$ $\xi = 1$	$\mapsto \xi$ $\xi = -1$ $\xi = 1$	$\mapsto \xi$ $\xi = -1$ $\xi = 1$
Type C	$\mapsto \xi$ $\xi = -1$ $\xi = 1$	$\mapsto \xi$ $\xi = -1$ $\xi = 1$	$\mapsto \xi$ $\xi = -1$ $\xi = 1$

Table 3 shows accuracy studies for the central deflection results of a simply supported homogeneous microplate obtained using our Hermitian C^2 DRKIM method with a uniform node distribution (i.e., Type A) and different values of the support size a_l and the l/h ratio. The microplate considered here is subjected to the same loads as used in Table 1. The relevant parameters are $l/h = 0, 0.1, 0.2, 0.3, 0.4,$ and 0.5; $L_x = L_y$ and $L_x/h = 5$; $n = 5$, $n_p = 21$. It can be seen in Table 3 that the solutions obtained using the current DRKIM method with the support sizes $3.5\Delta z \leq a_l \leq 6.5\Delta z$ closely agree with the 3D MCST results [50] and the CCST-based FLM results [51]. The relative errors between the solutions obtained using the current DRKIM method and the relevant 3D solutions increase when the support size is smaller than $a_l = 3.5\Delta z$ and is larger than $a_l = 6.5\Delta z$. Among these values of the support size a_l considered in Table 3, the selection of $a_l = 5.1\Delta z$ leads to a satisfactory result through the range of the l/h from $l/h = 0$ to $l/h = 0.5$, which is consistent with the guidance recommended by Chen et al. [45] and Wang et al. [46].

Table 3: Accuracy studies for the central deflection results of a simply supported homogeneous microplate obtained using our Hermitian C^2 DRKIM method with a uniform node distribution and different values of the support size a_l and the l/h ratio

a_l	$\hat{l}/h = 0$ ($l/h = 0$)	$\hat{l}/h = 0.2$ ($l/h = 0.1$)	$\hat{l}/h = 0.4$ ($l/h = 0.2$)	$\hat{l}/h = 0.6$ ($l/h = 0.3$)	$\hat{l}/h = 0.8$ ($l/h = 0.4$)	$\hat{l}/h = 1.0$ ($l/h = 0.5$)
$2.7\ \Delta z$	0.32466	0.28220	0.19897	0.13506	0.09530	0.07091
$2.9\ \Delta z$	0.32469	0.28406	0.19857	0.13505	0.09530	0.07094
$3.1\ \Delta z$	0.33231	0.28518	0.19844	0.13505	0.09530	0.07092
$3.3\ \Delta z$	0.33511	0.28495	0.19891	0.13506	0.09530	0.07089
$3.5\ \Delta z$	0.33554	0.28146	0.19871	0.13507	0.09530	0.07090
$3.7\ \Delta z$	0.33560	0.28788	0.19937	0.13510	0.09531	0.07091
$3.9\ \Delta z$	0.33576	0.28740	0.19947	0.13513	0.09532	0.07091
$4.1\ \Delta z$	0.33594	0.28498	0.19901	0.13505	0.09530	0.07090
$4.3\ \Delta z$	0.33611	0.28450	0.19900	0.13504	0.09529	0.07090
$4.5\ \Delta z$	0.33617	0.28441	0.19900	0.13505	0.09529	0.07090
$4.7\ \Delta z$	0.33615	0.28433	0.19899	0.13504	0.09529	0.07090

(Continued)

Table 3 (continued)

a_l	$\hat{l}/h = 0$ ($l/h = 0$)	$\hat{l}/h = 0.2$ ($l/h = 0.1$)	$\hat{l}/h = 0.4$ ($l/h = 0.2$)	$\hat{l}/h = 0.6$ ($l/h = 0.3$)	$\hat{l}/h = 0.8$ ($l/h = 0.4$)	$\hat{l}/h = 1.0$ ($l/h = 0.5$)
$4.9\,\Delta z$	0.33612	0.28427	0.19898	0.13504	0.09529	0.07090
$5.1\,\Delta z$	0.33609	0.28411	0.19896	0.13504	0.09529	0.07090
$5.3\,\Delta z$	0.33608	0.28387	0.19893	0.13503	0.09529	0.07090
$5.5\,\Delta z$	0.33606	0.28376	0.19891	0.13503	0.09529	0.07090
$5.7\,\Delta z$	0.33603	0.28379	0.19891	0.13503	0.09529	0.07090
$5.9\,\Delta z$	0.33601	0.28387	0.19889	0.13503	0.09529	0.07090
$6.1\,\Delta z$	0.33600	0.28404	0.19886	0.13502	0.09529	0.07090
$6.3\,\Delta z$	0.33601	0.28414	0.19882	0.13501	0.09529	0.07090
$6.5\,\Delta z$	0.33604	0.28418	0.19879	0.13501	0.09529	0.07090
$6.7\,\Delta z$	0.33609	0.28425	0.19878	0.13512	0.09532	0.07090
$6.9\,\Delta z$	0.33613	0.28447	0.19878	0.13511	0.09532	0.07090
$7.1\,\Delta z$	0.33617	0.28474	0.19877	0.13508	0.09531	0.07090
$7.3\,\Delta z$	0.33619	0.28459	0.19874	0.13506	0.09530	0.07090
3D MCST [50]	0.3357	0.2851	0.1991	0.1351	0.0953	0.0709
3D CCST-based FEM [51]	0.3357	0.2851	0.1991	0.1351	0.0953	0.0709
MCST-based RSDT [23]	0.3433	0.2875	0.1934	0.1251	0.0838	0.0588

Table 4 shows that the comparisons of the central deflection results of a simply-supported FG microplate obtained using our Hermitian C^2 DRKIM method with $n_p = 31$ and $n = 5$, the 3D CCST-based FEM [51], the refined quasi-3D IGAT [39], the MCST- and CCST-based RSDTs [23,27], and the CCST-based CPT [27]. The relevant geometric parameters are given as $L_x/h = 5$ and 20 and $L_x = L_y$. The relevant material parameters are $\hat{l}/h = 0, 0.2, 0.4,$ and 0.8 and $\kappa_p = 0, 1,$ and 10.

The loading conditions considered here are sinusoidally distributed loads and uniform loads and are expressed as follows:

For the sinusoidal type load,

$$\overline{q}_z^+ (x,\ y) = q_0 \sin\left(\pi x/L_x\right)\sin\left(\pi y/L_y\right), \tag{70a}$$

$$\overline{q}_z^- (x,\ y) = 0; \tag{70b}$$

For the uniform-type load,

$$\overline{q}_z^+ (x,\ y) = q_0$$
$$= \sum_{\hat{m}=1,3,\dots}^{n_{\hat{m}}} \sum_{\hat{n}=1,3,\dots}^{n_{\hat{n}}} 16 q_0 / \left(\hat{m}\hat{n}\pi^2\right), \tag{71a}$$

$$\text{and } \overline{q}_z^- (x,\ y) = 0, \tag{71b}$$

where in the following analysis, the convergent solutions are yielded when the values of $n_{\hat{m}}$ and $n_{\hat{n}}$ are taken to be $n_{\hat{m}} = n_{\hat{n}} = 29$.

As previously mentioned, the microplate is made of Al_2O_3 and Al materials, and their volume fractions are given in Eqs. (66a) and (66b). Table 4 shows the Hermitian C^2 DRKIM method's results

closely agree with those obtained using the 3D CCST-based FEM [51] and the quasi-3D IGAT [39]. It can be seen in Table 4 that the FG microplate's central deflection decreases when the value of the material length-scale parameter rises, indicating that an increase in the material length-scale parameter stiffens the microscale plate, decreasing its central deflection. The central deflection increases when the value of the inhomogeneity index (κ_p) rises, indicating that an increase in the value κ_p softens the microplate because the stiffer ceramic material's volume fraction will decrease as compared to the softer metal material's volume fraction, increasing the microplate's central deflection.

Table 5 shows the comparisons for the results of the FG microplate's in-plane stresses and deflections obtained using various 2D microstructure-dependent shear deformation theories on the basis of the MCST/CCST and our Hermitian C^2 DRKIM method. The relevant material parameters are $\kappa_p = 1$ and 10; and $\hat{l}/h = 0, 0.2, 0.5,$ and 1. The relevant geometric parameters are $L_x/h = 10$ and $L_x = L_y$. It can be seen in Table 5 that the solutions obtained using our Hermitian C^2 DRKIM method closely agree with those obtained using the 3D CCST-based FEM [51] and are more accurate than those of 2D microstructure-dependent shear deformation theories. In addition, the in-plane stress solutions decrease when the value of l rises, indicating that an increase in the value of l stiffens the microplate, resulting in fewer deformations and fewer in-plane stresses induced in the microplate. Due to its excellent performance, we apply the Hermitian C^2 DRKIM method to the following parametric study.

4.2 Parametric Study

This section presents a parametric study to understand the impact of essential factors on deformations, in-plane stresses, transverse stresses, and couple stresses induced in an EG microplate, which is placed under full simple supports and is subjected to mechanical loads. The microplate considered here is subjected to the sinusoidally distributed loads, which are $\overline{q}_z^+ = q_0 \sin(\pi x/L_x) \sin(\pi y/L_y)$ and $\overline{q}_z^- = 0$. Material properties of the microplate are assumed to obey an exponential law, exponentially varying in the thickness direction as follows:

$$E(z) = E_b\, e^{\kappa_e[1/2 + (z/h)]}, \tag{72a}$$

$$\upsilon(z) = 0.3, \tag{72b}$$

where $E_b = 70$ Gpa. When $z = h/2$, Eq. (72a) leads to $E_t = E_b\, e^{\kappa_e}$ and $\kappa_e = \ln \hat{\kappa}_e$, in which $\hat{\kappa}_e = E_t/E_b$. The symbols $\hat{\kappa}_e$ and κ_e are defined as the inhomogeneity index and its logarithm form. The subscripts b and t stand for the bottom and top surfaces of the microplate. When the value of $\hat{\kappa}_e$ is one (i.e., the value of κ_e is zero), the FG microplate is a homogeneous plate.

The dimensionless variables used in the following study are given as

$$(\overline{u},\ \overline{w}) = (u_x,\ u_\zeta)\left[10 E_b h^3/(q_0 L_x^4)\right]; \tag{73a}$$

$$\overline{\sigma}_{ij} = \sigma_{ij}\, h/(q_0 L_x) \qquad i, j = x,\ y,\ \text{and}\ \zeta, \quad \text{except}\ \overline{\sigma}_{\zeta\zeta} = \sigma_{\zeta\zeta}/q_0; \tag{73b}$$

$$(\overline{\mu}_x,\ \overline{\mu}_y,\ \overline{\mu}_\zeta) = \left[\mu_x/(q_0 L_x),\ \mu_y/(q_0 L_x),\ \mu_\zeta/(q_0 h)\right]. \tag{73c}$$

It is important to note that using dimensionless variables in the following analysis allows for a more comprehensive understanding of the results. For instance, when the value of the l/h ratio is fixed, like $l/h = d$, as we change the value of l and let $h = l/d$, or we change the value of h and let $l = (hd)$, we always obtain the same results. This approach enhances the robustness and applicability of our findings.

Table 4: Comparisons of the central deflection results of a simply supported FG microplate obtained using various MCST-/CCST-based microplate theories and our Hermitian C^2 DRKIM method

Loading-type	L_x/h	Theories	$\kappa_p = 0$				$\kappa_p = 1$				$\kappa_p = 10$			
			$\hat{l}/h=0$ $(l/h=0)$	$\hat{l}/h=0.2$ $(l/h=0.1)$	$\hat{l}/h=0.4$ $(l/h=0.2)$	$\hat{l}/h=0.8$ $(l/h=0.4)$	$\hat{l}/h=0$ $(l/h=0)$	$\hat{l}/h=0.2$ $(l/h=0.1)$	$\hat{l}/h=0.4$ $(l/h=0.2)$	$\hat{l}/h=0.8$ $(l/h=0.4)$	$\hat{l}/h=0$ $(l/h=0)$	$\hat{l}/h=0.2$ $(l/h=0.1)$	$\hat{l}/h=0.4$ $(l/h=0.2)$	$\hat{l}/h=0.8$ $(l/h=0.4)$
Sinusoidal-type	5	Hermitian C^2 DRKIM method	0.33571	0.28489	0.19912	0.09530	0.66202	0.54620	0.36524	0.16557	1.21969	1.0421	0.74093	0.36389
		3D CCST-based FEM [51]	0.3357	0.2851	0.1991	0.0953	0.6622	0.5476	0.3653	0.1656	1.2194	1.0394	0.7388	0.3636
		Quasi-3D IGAT [39]	0.3360	0.2853	0.1965	0.0879	0.6401	0.5321	0.3537	0.1520	1.1663	1.0019	0.7043	0.3220
		CCST-based RSDT [27]	0.3433	0.2875	0.1934	0.0838	0.6688	0.5468	0.3535	0.1464	1.2276	1.0247	0.6908	0.3052
		MCST-based RSDT [23]	0.3433	0.2875	0.1934	0.0838	0.6688	0.5468	0.3535	0.1464	1.2276	1.0247	0.6908	0.3052
		CCST-based CPT [27]	0.2803	0.2399	0.1676	0.0760	0.5623	0.4687	0.3127	0.1341	0.9355	0.8171	0.5922	0.2819
Sinusoidal-type	20	Hermitian C^2 DRKIM method	0.28377	0.24283	0.16964	0.07727	0.56859	0.47267	0.31612	0.13621	0.95343	0.83373	0.60407	0.28786
		3D CCST-based FEM [51]	0.2838	0.2428	0.1697	0.0773	0.5686	0.4738	0.3161	0.1362	0.9353	0.8315	0.6020	0.2875
		Quasi-3D IGAT [39]	0.2836	0.2427	0.1694	0.0768	0.5516	0.4619	0.3105	0.1343	0.9280	0.8120	0.5906	0.2825
		CCST-based RSDT [27]	0.2842	0.2430	0.1693	0.0765	0.5689	0.4737	0.3153	0.1349	0.9358	0.8303	0.5986	0.2834
		MCST-based RSDT [23]	0.2842	0.2430	0.1693	0.0765	0.5689	0.4737	0.3153	0.1349	0.9538	0.8303	0.5986	0.2834
		CCST-based CPT [27]	0.2803	0.2399	0.1676	0.0760	0.5623	0.4687	0.3127	0.1341	0.9355	0.8171	0.5922	0.2819
Uniform-type	5	Hermitian C^2 DRKIM method	0.57580	0.48699	0.33953	0.16287	1.13252	0.93087	0.62077	0.28196	2.10858	1.78839	1.26433	0.61984
		3D CCST-based FEM [51]	0.57593	0.48742	0.33953	0.16286	1.13273	0.93322	0.62082	0.28194	2.10957	1.78445	1.26062	0.61934
Uniform-type	20	Hermitian C^2 DRKIM method	0.47579	0.40710	0.28439	0.12963	0.95313	0.79224	0.52985	0.22847	1.60053	1.39907	1.01338	0.48314
		3D CCST-based FEM [51]	0.47579	0.40711	0.28444	0.12963	0.95316	0.79414	0.52984	0.22846	1.60066	1.39528	1.00984	0.48257

Table 5: Comparisons of the results for the deflections and stresses of a power-law-type FG square microplate with full simple supports obtained using various MCST-/CCST-based plate theories and our Hermitian C^2 DRKIM method

Deflection and stress parameters	Theories	$\kappa_p = 1$				$\kappa_p = 10$			
		$\hat{l}/h = 0$ $(l/h = 0)$	$\hat{l}/h = 0.2$ $(l/h = 0.1)$	$\hat{l}/h = 0.5$ $(l/h = 0.25)$	$\hat{l}/h = 1$ $(l/h = 0.5)$	$\hat{l}/h = 0$ $(l/h = 0)$	$\hat{l}/h = 0.2$ $(l/h = 0.1)$	$\hat{l}/h = 0.5$ $(l/h = 0.25)$	$\hat{l}/h = 1$ $(l/h = 0.5)$
$\bar{w}(L_x/2, L_y/2, 0)$	Hermitian C^2 DRKIM method	0.58748	0.48761	0.26177	0.10125	1.00736	0.87895	0.52728	0.22155
	3D CCST-based FEM [51]	0.5875	0.4888	0.2617	0.1012	1.0073	0.8734	0.5228	0.2212
	CCST-based SSDT [27]	0.5889	0.4884	0.2576	0.0959	1.0089	0.8704	0.5085	0.2060
	CCST-based RSDT [27]	0.5890	0.4885	0.2577	0.0959	1.0087	0.8697	0.5079	0.2058
	MCST-based RSDT [23]	0.5890	0.4885	NA	0.0959	1.0087	0.8697	NA	0.2058
	CCST-based CPT [27]	0.5623	0.4687	0.2502	0.0939	0.9355	0.8171	0.4909	0.2024
$\bar{\sigma}_x(L_x/2, L_y/2, h/2)$	Hermitian C^2 DRKIM method	3.09777	2.56383	1.35966	0.50460	5.06617	4.41609	2.60790	1.02346
	3D CCST-based FEM [51]	3.0973	2.5701	1.3592	0.5044	5.0633	4.3906	2.5857	1.0205
	CCST-based SSDT [27]	3.0870	2.5613	1.3530	0.5044	5.0890	4.4135	2.6158	1.0727
	CCST-based RSDT [27]	3.0850	2.5598	1.3524	0.5042	5.0849	4.4103	2.6156	1.0733
	MCST-based RSDT [23]	3.0870	2.5541	1.3467	0.5048	5.0890	4.4019	2.6050	1.0737
	CCST-based CPT [27]	3.0537	2.5456	1.3588	0.5099	5.0173	4.3824	2.6330	1.0855
$\bar{\tau}_{xy}(0, 0, -h/3)$	Hermitian C^2 DRKIM method	0.61106	0.50674	0.26889	0.09893	0.59262	0.51853	0.30909	0.12391
	3D CCST-based FEM [51]	0.6112	0.5081	0.2689	0.0989	0.5927	0.5156	0.3065	0.1237
	CCST-based SSDT [27]	0.6110	0.5071	0.2680	0.1000	0.5894	0.5120	0.3049	0.1255
	CCST-based RSDT [27]	0.6111	0.5072	0.2681	0.1000	0.5896	0.5123	0.3053	0.1257
	MCST-based RSDT [23]	0.6110	0.5061	0.2677	0.1007	0.5894	0.5111	0.3044	0.1262
	CCST-based CPT [27]	0.6125	0.5106	0.2726	0.1023	0.5926	0.5176	0.3110	0.1282

Fig. 4a–h shows the variations in dimensionless displacements, in-plane stresses, transverse stresses, and couple stresses induced in an EG microplate along the thickness direction, with the values of the inhomogeneity index ($\hat{\kappa}_e$) being 1, 5, and 10. The relevant material parameters are $l/h = 0.5$ and $l = 8.8 \times 10^{-6}$ m. The relevant geometric parameters are $L_x/h = 10$ and $L_x/L_y = 1$. The results in Fig. 4b show that the microplate's overall stiffness increases when the value of $\hat{\kappa}_e$ rises, decreasing the microplate's deflection. The results in Fig. 4c and d show that the in-plane normal and shear stress distributions along the thickness direction look like higher-order polynomial functions for an EG microplate ($\hat{\kappa}_e \neq 1$); however, these distributions look like linear functions for a homogeneous microplate ($\hat{\kappa}_e = 1$). Fig. 4e and f shows that the transverse shear and normal stress distributions along the thickness direction look like higher-order polynomial functions in an EG microplate, and the pick value occurs in the upper half of the microplate; however, these distributions appear to be parabolic functions in a homogeneous microplate with the pick value occurring at the microplate's mid-plane. Fig. 4g and h shows that the couple stress distribution along the thickness direction looks like higher-order polynomial functions. The variations in the induced stress and deformation distributions along the thickness direction for an FG microplate are more significant than those for a homogeneous microplate.

Fig. 5a–h shows the variations in the dimensionless displacement, in-plane stresses, transverse stresses, and couple stresses induced in an EG microplate along the thickness direction, with the values of the l/h ratio being 0, 0.2, and 0.4. The other material parameter is $\kappa_e = 2$; and the relevant geometric parameters are $L_x/L_y = 1$, $L_x/h = 10$, and $h = 1 \times 10^{-6}$ m.
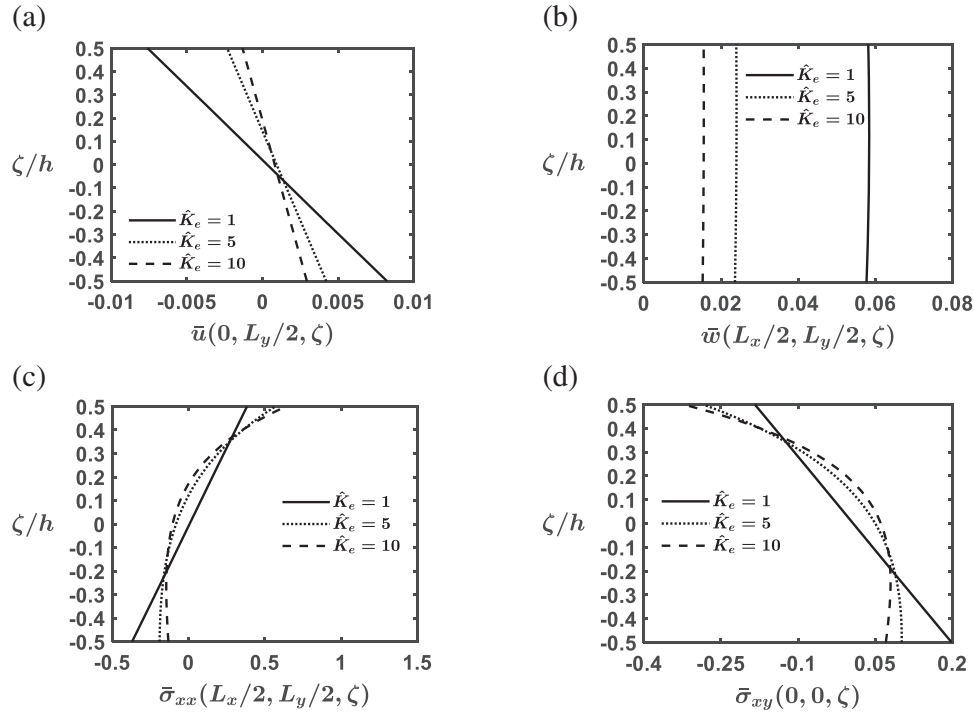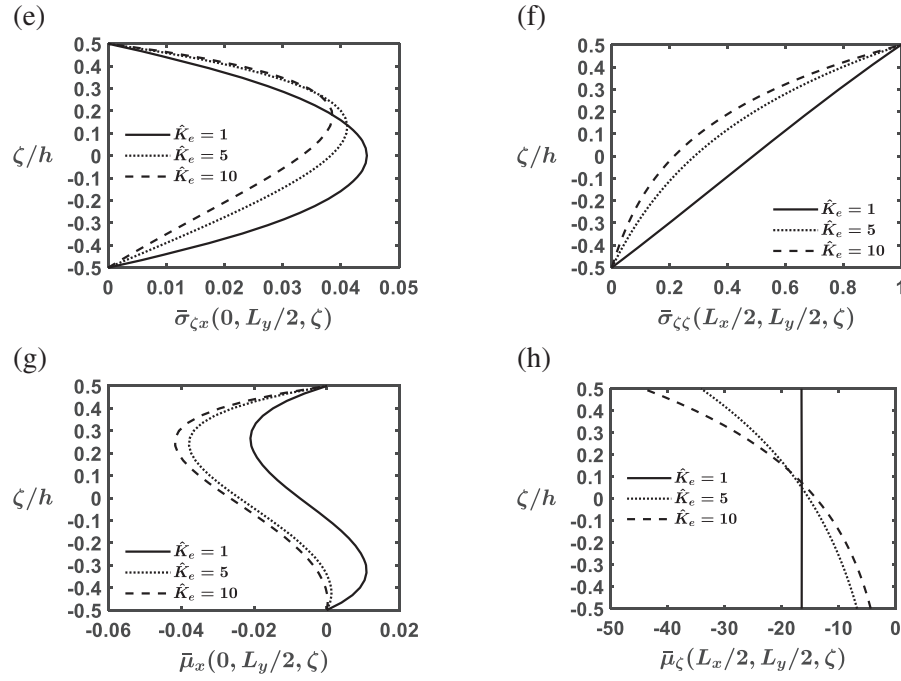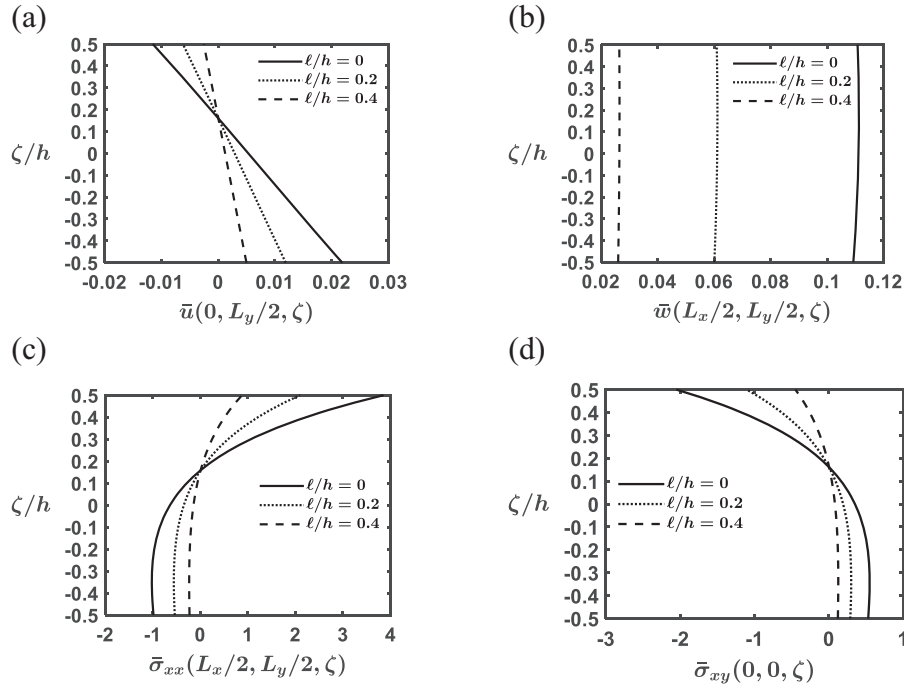
(a)

(b)

(c)
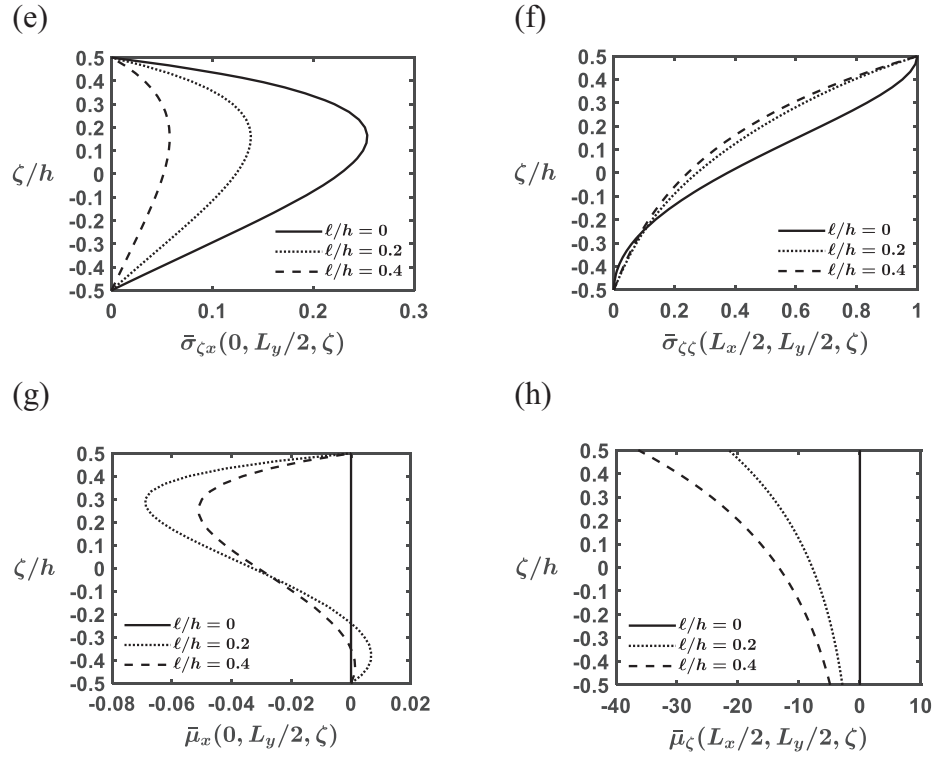
(d)

Figure 4: (Continued)

Figure 4: Variations in the dimensionless (a) in-plane displacement $\overline{u}$, (b) out-of-plane displacement $\overline{w}$, (c) in-plane normal stress $\overline{\sigma}_{xx}$, (d) in-plane shear stress $\overline{\sigma}_{xy}$, (e) transverse shear stress $\overline{\sigma}_{\zeta x}$, (f) transverse normal stress $\overline{\sigma}_{\zeta\zeta}$, (g) couple stress $\overline{\mu}_x$, and (h) couple stress $\overline{\mu}_\zeta$ along the thickness direction, with the value of the inhomogeneity index being 1, 5, and 10

Figure 5: (Continued)

Figure 5: Variations in the dimensionless (a) in-plane displacement $\overline{u}$, (b) out-of-plane displacement $\overline{w}$, (c) in-plane normal stress $\overline{\sigma}_{xx}$, (d) in-plane shear stress $\overline{\sigma}_{xy}$, (e) transverse shear stress $\overline{\sigma}_{\zeta x}$, (f) transverse normal stress $\overline{\sigma}_{\zeta\zeta}$, (g) couple stress $\overline{\mu}_x$, and (h) couple stress $\overline{\mu}_\zeta$ along the thickness direction, with the value of the l/h ratio being 0, 0.2, and 0.4

It can be seen in Fig. 5b that an increase in the value of l stiffens the microplate, leading to its deflection decrease. The results in Fig. 5c–f show that the variations in the in-plane stress and transverse stress induced in the microplate along its thickness direction with a smaller value of l are more significant than those induced in the microplate along the thickness direction with a more considerable value of l. This is because an increase in the value of l stiffens the microplate, which leads to fewer deformations and fewer stresses induced in the microplate when the magnitude of the applied load remains constant. The results in Fig. 5g and h show that the variations in the couple stresses ($\overline{\mu}_x$ and $\overline{\mu}_\zeta$) along the thickness coordinate look like higher-order polynomial functions.

Fig. 6a–h shows that the variations in the dimensionless deformations, in-plane stresses, transverse stresses, and couple stresses induced in an EG microplate along the thickness direction, with the length-to-thickness ratios being 5, 10, and 20. The relevant material parameters are $l/h = 0.5$ and $l = 8.8 \times 10^{-6}$ m. The dimensionless displacements are redefined as $(\overline{u},\ \overline{w}) = (u_x,\ u_\zeta)\,[10E_b/(q_0 h)]$. The results in Fig. 6a and b show that the microplate's overall stiffness decreases when the value of the L_x/h ratio rises, increasing its deflection. The results in Fig. 6c–f show that the variations in the in-plane stresses and transverse stresses induced in the microplate along the thickness direction with a more considerable value of the L_x/h ratio are more significant than those induced in the microplate along the thickness direction with a smaller value of the L_x/h ratio. This is because a decrease in the value of the L_x/h ratio stiffens the microplate, leading to fewer deformations and fewer stresses induced in the microplate when the magnitude of the applied load remains constant.
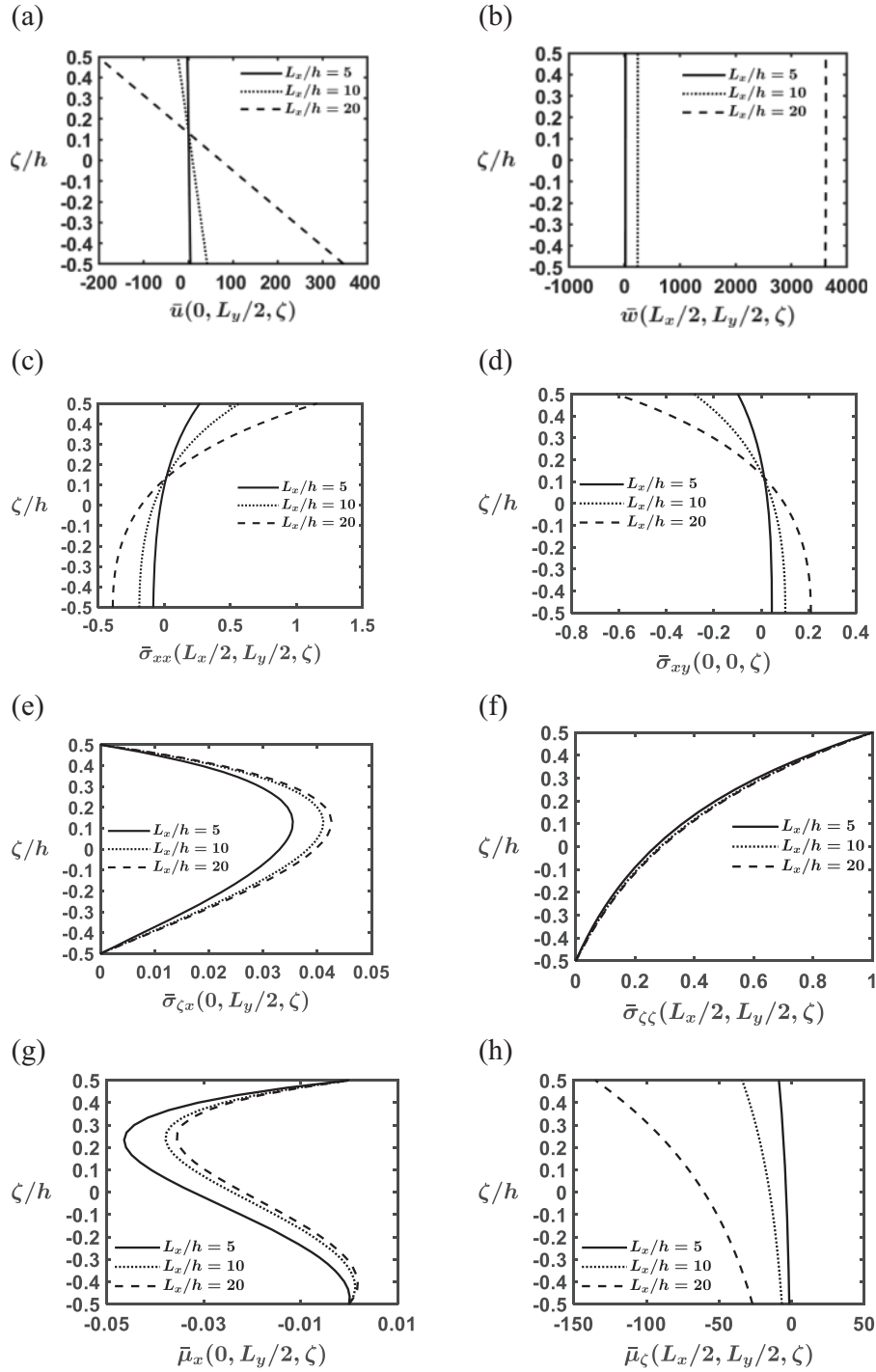
Figure 6: Variations in the dimensionless (a) in-plane displacement $\bar{u}$, (b) out-of-plane displacement $\bar{w}$, (c) in-plane normal stress $\bar{\sigma}_{xx}$, (d) in-plane shear stress $\bar{\sigma}_{xy}$, (e) transverse shear stress $\bar{\sigma}_{\zeta x}$, (f) transverse normal stress $\bar{\sigma}_{\zeta\zeta}$, (g) couple stress $\bar{\mu}_{x}$, and (h) couple stress $\bar{\mu}_{\zeta}$ along the thickness direction, with the values of the L_{x}/h ratio being 5, 10, and 20

5 Concluding Remarks

A Hermitian C^2 DRKIM method based on the strong form of the 3D CCST has been developed for analyzing the 3D microstructure-dependent static flexural behavior of an FG/EG microplate. The FG/EG microplate considered here was subjected to mechanical loads and placed under full simple supports. The unique features of this Hermitian C^2 DRK interpolant compared with the early Lagrange-type reproducing kernel interpolant for analyzing macroscale plate's mechanical behavior are that the displacements, the transverse stresses, and their first-order and second-order derivatives are selected as primary variables satisfying the nodal interpolation properties, and their corresponding shape functions satisfy the Kronecker delta properties. These features make our Hermitian C^2 DRKIM method suitable for analyzing the FG microplate's mechanical behavior because the deflections and rotations prescribed at the boundary edges of the microplate considered here can thus be directly imposed without using the penalty method, which is necessary for the conventional reproducing kernel point collocation method. In addition, using our Hermitian C^2 DRKIM method, the primary variables' higher-order derivatives involved in the strong form of the CCST can be effectively estimated.

In the validation and comparison study, the solutions obtained using our Hermitian C^2 DRKIM method closely agree with the available 3D solutions in the literature, with a fast convergence rate. Because the 3D couple stress effect is significant when the value of the l/h ratio rises, the performance of the Hermitian C^2 DRKIM method is superior to that of 2D CCST-/MCST-based shear deformation microplate theories, especially for the microplate with a considerable value of the l/h ratio. For example, the maximum relative error between the solutions obtained using the Hermitian C^2 DRKIM method and those obtained using the 3D MCST is 0.35% for a range of the value of the l/h ratio between $l/h = 0$ and $l/h = 0.5$, respectively; however, the relative error between the solutions obtained using the 2D RSDT and the 3D MCST solutions is 2.3% in the case of $l/h = 0$, and it increases up to 17.1% when the value of the l/h ratio is 0.5.

In the parametric study, we presented the displacement, in-plane stress, transverse stress, and couple stress distributions along the thickness direction of an EG microplate using our Hermitian C^2 DRKIM method. These distributions cannot be effectively estimated using existing 2D microstructure-dependent shear deformation theories, especially for the transverse stress and couple stress distributions, so they have yet to be shown in public literature. Thus, the parametric analysis results can provide a reference for assessing the accuracy of existing 2D microstructure-dependent shear deformation theories. Furthermore, the results are also helpful for making assumptions about primary variable components for an advanced microstructure-dependent shear deformation microplate theory, which is to be developed.

Author Contributions: Chih-Ping Wu: Conceptualization, Methodology, Validation, Formal analysis, Investigation, Resources, Data curation, Writing—original draft preparation, Writing—review and editing, Supervision, Project administration, Funding acquisition. Ruei-Syuan Chang: Software, Validation, Formal analysis, Investigation, Data curation. All authors reviewed the results and approved the final version of the manuscript.

Availability of Data and Materials: The processed data required to reproduce these findings can be downloaded from https://docs.google.com/document/d/1hvfVYcF5hsGj-4HEn4WOJL9y3hNq68Q/edit?usp=drive_link&ouid=103032847656566806520&rtpof=true&sd=true (accessed on 20 May 2024).

Conflicts of Interest: The authors declare they have no conflicts of interest to report regarding the current study.

References

1. Hossain MI, Masour S. A critical overview of thin films coating technologies for energy applications. Cogent Eng. 2023;10(1):2179467.
2. Sathish M, Radhika N. Current status, challenges, and future prospects of thin film costing techniques and coating structures. J Bio Tribo Corros. 2023;9:35.
3. Faudzi AAM, Sabzehmeidani Y, Suzumori K. Application of micro-electro-mechanical systems (MEMS) as sensors: a review. J Robot Mechatron. 2020;32(2):281–8.
4. Gilewski M. Micro-electro-mechanical systems in light stabilization. Sensors. 2023;23(6):2916.
5. Magazzu A, Marcuello C. Investigation of soft matter nanomechanics by atomic force microscopy and optical tweezers: a comprehensive review. Nanomater. 2023;13(6):963.
6. Liu Q, Fu Y, Qin Z, Wang Y, Zhang S, Ran M. Progress in the applications of atomic force microscope (AFM) for mineralogical research. Micro. 2023;170(1–3):103460. doi:10.1016/j.micron.2023.103460.
7. Lam DCC, Yang F, Chong ACM, Wang J, Tong P. Experiments and theory in strain gradient elasticity. J Mech Phys Solids. 2002;51(8):1477–508. doi:10.1016/S0022-5096(03)00053-X.
8. Soldatos KP. New trends in couple stress hyperelasticity. Math Mech Solids. 2023;67:108128652311776. doi:10.1177/10812865231177673.
9. Taghizadeh M, Babaei M, Dimitri R, Tornabene F. Assessment of critical buckling load of bi-directional functionally graded truncated conical micro-shells using modified couple stress theory and Ritz method. Mech Based Des Struct Mach. 2023;52(6):3456–87. doi:10.1080/15397734.2023.2202230.
10. Zhang Y, Cheng Z, Zhu T, Lu L. Mechanics of gradient nanostructured metals. J Mech Phys Solids. 2024;189:105719. doi:10.1016/j.jmps.2024.105719.
11. Jiang Y, Li L, Hu Y. Strain gradient elasticity theory of polymer networks. Acta Mech. 2022;233:3213–31.
12. Ferrari M, Granik VT, Imam A, Nadeau JC. Advances in doublet mechanics. Germany: Springer; 1997. p. 1–26.
13. Carrera E, Zozulya VV. Carrera unified formulation (CUF) for the micropolar plates and shells. I. Higher order theory. Mech Adv Mater Struct. 2020;29(6):773–95.
14. Carrera E, Zozulya VV. Carrera unified formulation (CUF) for the micropolar plates and shells. II. Complete linear expansion case. Mech Adv Mater Struct. 2020;29(6):796–815.
15. Eringen AC. Nonlocal continuum field theories. New York: Springer; 2002. p. 71–176.
16. Hadjesfandiari AR, Dargush GF. Couple stress theory for solids. Int J Solids Struct. 2011;48(18):2496–510.
17. Hadjesfandiari AR, Dargush GF. Fundamental solutions for isotropic size-dependent couple stress elasticity. Int J Solids Struct. 2013;50(9):1253–65.
18. Yang F, Chong ACM, Lam DCC, Tong P. Couple stress-based strain gradient theory for elasticity. Int J Solids Struct. 2002;39(10):2731–43. doi:10.1016/S0020-7683(02)00152-X.
19. Beni YT, Mehralian F, Zeighampour H. The modified couple stress functionally graded cylindrical thin shell formulation. Mech Adv Mater Struct. 2016;23(7):791–801. doi:10.1080/15376494.2015.1029167.

20. Ma HM, Gao XL, Reddy JN. A non-classical Mindlin plate model based on a modified couple stress theory. Acta Mech. 2011;220(1-4):217–35. doi:10.1007/s00707-011-0480-4.

21. Arefi M, Kiani M. Magneto-electro-mechanical bending analysis of three-layered exponentially graded microplate with piezomagnetic face sheets resting on Pasternak's foundation via MCST. Mech Adv Mater Struct. 2020;27(5):383–95. doi:10.1080/15376494.2018.1473538.

22. Lei J, He Y, Zhang B, Liu D, Shen L, Guo S. A size-dependent FG micro-plate model incorporating higher-order shear and normal deformation effects based on a modified couple stress theory. Int J Mech Sci. 2015;104(5):8–23. doi:10.1016/j.ijmecsci.2015.09.016.

23. Thai HT, Kim SE. A size-dependent functionally graded Reddy plate model based on a modified couple stress theory. Compos Part B. 2013;45(1):1636–45. doi:10.1016/j.compositesb.2012.09.065.

24. Kim J, Reddy JN. Analytical solutions for bending, vibration, and buckling of FGM plates using a couple stress-based third-order theory. Compos Struct. 2013;103(3):86–98. doi:10.1016/j.compstruct.2013.03.007.

25. Thai HT, Vo TP. A size-dependent functionally graded sinusoidal plate model based on a modified couple stress theory. Compos Struct. 2013;96(20):376–83. doi:10.1016/j.compstruct.2012.09.025.

26. Sobhy M, Zenkour AM. A comprehensive study on the size-dependent hygrothermal analysis of exponentially graded microplates on elastic foundations. Mech Adv Mater Struct. 2020;27(10):816–30. doi:10.1080/15376494.2018.1499986.

27. Wu CP, Hu HX. A unified size-dependent plate theory for static bending and free vibration analyses of micro- and nano-scale plates based on the consistent couple stress theory. Mech Mater. 2021;162:104085. doi:10.1016/j.mechmat.2021.104085.

28. Deng T, Zhang B, Liu J, Shen H, Zhang X. Vibration frequency and mode localization characteristics of strain gradient variable-thickness microplates. Thin-Walled Struct. 2024;199:111779.

29. Balobanov V, Kiendl J, Khakalo S, Niiranen J. Kirchhoff-Love shells within strain gradient elasticity: weak and strong formulations and an H^3-conforming isogeometric implementation. Comput Methods Appl Mech Eng. 2019;344:837–57.

30. Zhang B, Li H, Kong L, Zhang X, Feng Z. Strain gradient differential quadrature finite element for moderately thick micro-plates. Int J Numer Methods Eng. 2020;121(24):5600–46.

31. Thanh GE, Tran LV, Bui TQ, Nguyen HX, Abdel-Wahab M. Isogeometric analysis for size-dependent nonlinear thermal stability of porous FG microplates. Compos Struct. 2019;221:110838.

32. Nguyen NX, Atroshchenko E, Nguyen-Xuan H, Vo TP. Geometrically nonlinear isogeometric analysis of functionally graded microplates with the modified couple stress theory. Comput Struct. 2017;193:110–27.

33. Pham QH, Nguyen PC, Tran VK, Lieu QX, Tran TT. Modified nonlocal couple stress isogeometric approach for bending and free vibration analysis of functionally graded nanoplates. Eng Comput. 2023;39(1):993–1018. doi:10.1007/s00366-022-01726-2.

34. Wu CP, Tan TF, Hsu HT. A size-dependent finite element method for the 3D free vibration analysis of functionally graded graphene platelets-reinforced composite cylindrical microshells based on the consistent couple stress theory. Materials. 2023;16(6):2363. doi:10.3390/ma16062363.

35. Wu CP, Wu ML, Hsu HT. 3D size-dependent dynamic instability analysis of FG cylindrical microshells subjected to combinations of periodic axial compression and external pressure using a Hermitian C^2 finite layer method based on the consistent couple stress theory. Materials. 2024;17(4):810. doi:10.3390/ma17040810.

36. Roque CMC, Ferreira AJM, Reddy JN. Analysis of Mindlin microplates with a modified couple stress theory and a meshless method. Appl Math Modell. 2013;37(7):4626–33. doi:10.1016/j.apm.2012.09.063.

37. Tran TD, Thai CH, Nguyen-Xuan H. A size-dependent functionally graded higher-order plate analysis based on modified couple stress theory and moving Kriging meshfree method. Comput Mater Contin. 2018;57(3):447–83. doi:10.32604/cmc.2018.01738.

38. Thai CH, Ferreira AJM, Lee J, Nguyen-Xuan H. An efficient size-dependent computational approach for functionally graded isotropic and sandwich microplates based on modified couple stress theory and moving Kriging-based meshfree method. Int J Mech Sci. 2018;142–143:322–38.

39. Nguyen H, Nguyen TN, Abdel-Wahab M, Bordas SPA, Nguyen-Xuan H, Vo TP. A refined quasi-3D isogeometric analysis for functionally graded microplates based on the modified couple stress theory. Comput Methods Appl Mech Eng. 2017;313:904–40.

40. Thai CH, Ferreira AJM, Tran TD, Phung-Van P. A size-dependent quasi-3D isogeometric model for functionally graded graphene platelet-reinforced composite microplates based on the modified couple stress theory. Compos Struct. 2020;234:111695.

41. Li S, Lu H, Han W, Liu WK, Simkins DC. Reproducing kernel element method Part II: globally conforming I^m/C^n hierarchies. Comput Methods Appl Mech Eng. 2004;193:953–87.

42. Simkins Jr DC, Li S, Lu H, Liu WK. Reproducing kernel element method. Part IV: globally compatible C^n (n ≥ 1) triangular hierarchy. Comput Methods Appl Mech Eng. 2004;193:1013–34.

43. Liu WK, Han W, Lu H, Li S, Cao J. Reproducing kernel element method. Part I: theoretical formulation. Comput Methods Appl Mech Eng. 2004;193:933–51.

44. Lu H, Li S, Simkins Jr. DC, Liu WK, Cao J. Reproducing kernel element method Part III: generalized enrichment and applications. Comput Methods Appl Mech Eng. 2004;193:989–1011.

45. Chen SM, Wu CP, Wang YM. A Hermite DRK interpolation-based collocation method for the analyses of Bernoulli-Euler beams and Kirchhoff-Love plates. Comput Mech. 2011;47:425–53.

46. Wang YM, Chen SM, Wu CP. A meshless collocation method based on the differential reproducing kernel interpolation. Comput Mech. 2010;45:585–606.

47. Li S, Liu WK. Meshfree and particle methods and their applications. Appl Mech Rev. 2002;55(1):1–34.

48. Tang C, Alici G. Evaluation of length-scale effects for mechanical behavior of micro- and nanocantilevers: I. Experimental determination of length-scale factors. J Phys D: Appl Phys. 2011;44:335501.

49. Song J, Wei Y. A method to determine material length scale parameters in elastic strain gradient theory. J Appl Mech. 2020;87:031010.

50. Salehipour H, Nahvi H, Shahidi A, Mirdamadi HR. 3D elasticity analytical solution for bending of FG FG micro/nanoplates resting on elastic foundation using modified couple stress theory. Appl Math Modell. 2017;47:174–88.

51. Wu CP, Hsu CH. A three-dimensional weak formulation for stress, deformation, and free vibration analyses of functionally graded microscale plates based on the consistent couple stress theory. Compos Struct. 2022;296:115829.

Appendix A: The Higher-Order Derivative of the Hermitian C^2 DRK Interpolant

The rth-order derivative of the Hermitian C^2 DRK interpolant $f^h(\xi)$ with respect to ξ is expressed as follows:

$$\frac{d^r f^h(\xi)}{d\xi^r} = \sum_{l=1}^{n_p} \left[N_l^{(r)}(\xi) f_l + \hat{N}_l^{(r)}(\xi) \theta_l + \overline{N}_l^{(r)}(\xi) \kappa_l \right]$$

$$= \sum_{l=1}^{n_p} \left[\left(\phi_l^{(r)}(\xi) + \psi_l^{(r)}(\xi) \right) f_l + \left(\hat{\phi}_l^{(r)}(\xi) + \hat{\psi}_l^{(r)}(\xi) \right) \theta_l + \left(\overline{\phi}_l^{(r)}(\xi) + \overline{\psi}_l^{(r)}(\xi) \right) \kappa_l \right], \qquad (74)$$

where $N_l^{(r)}(\xi)$, $\hat{N}_l^{(r)}(\xi)$, and $\overline{N}_l^{(r)}(\xi)$ are the shape functions of Hermitian C^2 DRK interpolant's rth-order derivatives at the sampling node $\xi = \xi_l$; $\psi_l^{(r)}(\xi)$, $\hat{\psi}_l^{(r)}(\xi)$, and $\overline{\psi}_l^{(r)}(\xi)$ $(l = 1, 2, \ldots, n_p)$ denote primitive functions' rth-order derivatives (i.e., $\psi_l^{(r)}(\xi) = d^r \psi_l(\xi)/d\xi^r$, $\hat{\psi}_l^{(r)}(\xi) = d^r \hat{\psi}_l(\xi)/d\xi^r$,

and $\overline{\psi}_l^{(r)}(\xi) = d^r \overline{\psi}_l(\xi)/d\xi^r$); and $\phi_l^{(r)}(\xi)$, $\hat{\phi}_l^{(r)}(\xi)$, and $\overline{\phi}_l^{(r)}(\xi)$ ($l = 1, 2, \ldots, n_p$) denote enrichment functions' rth-order derivatives, which are obtained by imposing the nth-order DRCs, and are given by $\phi_l^{(r)}(\xi) = w_a(\xi - \xi_l)\mathbf{P}^T(\xi - \xi_l)\mathbf{b}_r^{c2}(\xi)$, $\hat{\phi}_l^{(r)}(\xi) = w_a(\xi - \xi_l)\hat{\mathbf{P}}^T(\xi - \xi_l)\mathbf{b}_r^{c2}(\xi)$, and $\overline{\phi}_l^{(r)}(\xi) = w_a(\xi - \xi_l)\overline{\mathbf{P}}^T(\xi - \xi_l)\mathbf{b}_r^{c2}(\xi)$, in which $\mathbf{b}_r^{c2}(\xi)$ is the undetermined function vector.

The undetermined functions $\mathbf{b}_r^{c2}(\xi)$ in Eq. (74) can be determined by selecting the complete nth-order polynomials as the basis functions to be reproduced and set up $(n + 1)$ DRCs as follows:

$$\sum_{l=1}^{np} \mathbf{P}(\xi - \xi_l)\ \phi_l^{(r)}(\xi) + \sum_{l=1}^{np} \hat{\mathbf{P}}(\xi - \xi_l)\ \hat{\phi}_l^{(r)}(\xi) + \sum_{l=1}^{np} \overline{\mathbf{P}}(\xi - \xi_l)\ \overline{\phi}_l^{(r)}(\xi)$$
$$= d^r\mathbf{P}(0)/d\xi_l^r - \sum_{l=1}^{np} \mathbf{P}(\xi - \xi_l)\ \psi_l^{(r)}(\xi) - \sum_{l=1}^{np} \hat{\mathbf{P}}(\xi - \xi_l)\ \hat{\psi}_l^{(r)}(\xi) - \sum_{l=1}^{np} \overline{\mathbf{P}}(\xi - \xi_l)\ \overline{\psi}_l^{(r)}(\xi). \tag{75}$$

We substitute the enrichment functions in Eq. (74) into the differential reproducing conditions in Eq. (75). As a result, we obtain the undetermined function vector $\mathbf{b}_r^{c2}(\xi)$ as follows:

$$\mathbf{b}_r^{c2}(\xi) = \mathbf{A}_{c2}^{-1}(\xi)\left[d^r\mathbf{P}(0)/d\xi_l^r - \sum_{l=1}^{np} \mathbf{P}(\xi - \xi_l)\ \psi_l^{(r)}(\xi) - \sum_{l=1}^{np} \hat{\mathbf{P}}(\xi - \xi_l)\ \hat{\psi}_l^{(r)}(\xi)\right.$$
$$\left. - \sum_{l=1}^{np} \overline{\mathbf{P}}(\xi - \xi_l)\ \overline{\psi}_l^{(r)}(\xi)\right]. \tag{76}$$

We substitute Eq. (76) into Eq. (74) to obtain the shape functions of Hermitian C^2 DRK interpolant's rth-order derivatives as follows:

$$N_l^{(r)}(\xi) = \phi_l^{(r)}(\xi) + \psi_l^{(r)}(\xi) \qquad (l = 1, 2, \ldots, n_p), \tag{77}$$

$$\hat{N}_l^{(r)}(\xi) = \hat{\phi}_l^{(r)}(\xi) + \hat{\psi}_l^{(r)}(\xi) \qquad (l = 1, 2, \ldots, n_p), \tag{78}$$

$$\overline{N}_l^{(r)}(\xi) = \overline{\phi}_l^{(r)}(\xi) + \overline{\psi}_l^{(r)}(\xi) \qquad (l = 1, 2, \ldots, n_p), \tag{79}$$

where

$$\phi_l^{(r)}(\xi) = w_a(\xi - \xi_l)\mathbf{P}^T(\xi - \xi_l)\mathbf{b}_r^{c2}(\xi),\ \hat{\phi}_l^{(r)}(\xi) = w_a(\xi - \xi_l)\hat{\mathbf{P}}^T(\xi - \xi_l)\mathbf{b}_r^{c2}(\xi),\ \overline{\phi}_l^{(r)}(\xi) = w_a(\xi - \xi_l)\overline{\mathbf{P}}^T(\xi - \xi_l)\mathbf{b}_r^{c2}(\xi).$$

Appendix B: The Relevant Coefficients $\tilde{d}_{ij}$

The relevant coefficients $\tilde{d}_{ij}$ are given as follows:

$\tilde{d}_{11} = G_{32}c_{55}^{-1}l^2,\ \tilde{d}_{12} = G_{32,z}\ c_{55}^{-1}l^2,\ \tilde{d}_{13} = -\left(\tilde{m}^2 G_{21} + \tilde{n}^2 G_{32}\right)c_{55}^{-1}l^2 - 1,\ \tilde{d}_{14} = -\tilde{n}^2 G_{32,z}\ c_{55}^{-1}l^2,$

$\tilde{d}_{15} = \tilde{m}\tilde{n}\left(G_{32} - G_{21}\right)c_{55}^{-1}l^2,\ \tilde{d}_{16} = \tilde{m}\tilde{n}G_{32,z}\ c_{55}^{-1}l^2,\ \tilde{d}_{17} = -\tilde{m}G_{32}c_{55}^{-1}l^2,\ \tilde{d}_{18} = -\tilde{m}G_{32,z}\ c_{55}^{-1}l^2,$

$\tilde{d}_{19} = \left(\tilde{m}^3 + \tilde{m}\tilde{n}^2\right)G_{21}c_{55}^{-1}l^2 - \tilde{m},\ \tilde{d}_{110} = c_{55}^{-1},\ \tilde{d}_{21} = \tilde{m}\tilde{n}\left(G_{13} - G_{21}\right)c_{44}^{-1}l^2,\ \tilde{d}_{22} = \tilde{m}\tilde{n}G_{13,z}\ c_{44}^{-1}l^2,$

$\tilde{d}_{23} = G_{13}c_{44}^{-1}l^2,\ \tilde{d}_{24} = G_{13,z}\ c_{44}^{-1}l^2,\ \tilde{d}_{25} = -\left(\tilde{m}^2 G_{13}c_{44}^{-1} + \tilde{n}^2 G_{21}c_{44}^{-1}\right)l^2 - 1,\ \tilde{d}_{26} = -\tilde{m}^2 G_{13,z}\ c_{44}^{-1}l^2,\ \tilde{d}_{27} = -\tilde{n}G_{13}c_{44}^{-1}l^2,\ \tilde{d}_{28} = -\tilde{n}G_{13,z}\ c_{44}^{-1}l^2,\ \tilde{d}_{29} = \left(\tilde{m}^2\tilde{n} + \tilde{n}^3\right)G_{21}c_{44}^{-1}l^2 - \tilde{n},\ \tilde{d}_{210} = c_{44}^{-1},\ \tilde{d}_{31} = \tilde{m}\tilde{c}_{13},$

$\tilde{d}_{32} = \tilde{n}\tilde{c}_{23},\ \tilde{d}_{33} = c_{33}^{-1},\ \tilde{d}_{41} = -\tilde{n}^2 G_{32}l^2,\ \tilde{d}_{42} = \left(\tilde{m}^2 Q_{11} + \tilde{n}^2 c_{66}\right) + \left(\tilde{m}^2\tilde{n}^2 G_{13} + \tilde{n}^4 G_{32}\right)l^2,\ \tilde{d}_{43} = \tilde{m}\tilde{n}G_{13}l^2,$

$\tilde{d}_{44} = \tilde{m}\tilde{n}\left(Q_{12} + c_{66}\right) - \left(\tilde{m}^3\tilde{n}G_{13} + \tilde{m}\tilde{n}^3 G_{32}\right)l^2,\ \tilde{d}_{45} = \left(-\tilde{m}\tilde{n}^2 G_{13} + \tilde{m}\tilde{n}^2 G_{32}\right)l^2,\ \tilde{d}_{46} = -\tilde{m}\tilde{c}_{13},$

$$\tilde{d}_{51} = \tilde{m}\tilde{n}G_{32}l^2, \tilde{d}_{52} = \tilde{m}\tilde{n}\left(Q_{12} + c_{66}\right) - \left(\tilde{m}\tilde{n}^3G_{32} + \tilde{m}^3\tilde{n}G_{13}\right)l^2, \tilde{d}_{53} = -\tilde{m}^2G_{13}l^2,$$

$$\tilde{d}_{54} = \left(\tilde{n}^2Q_{22} + \tilde{m}^2c_{66}\right) + \left(\tilde{m}^2\tilde{n}^2G_{32} + \tilde{m}^4G_{13}\right)l^2, \tilde{d}_{55} = \left(\tilde{m}^2\tilde{n}G_{13} - \tilde{m}^2\tilde{n}G_{32}\right)l^2, \tilde{d}_{56} = -\tilde{n}\tilde{c}_{23},$$

$$\tilde{d}_{61} = 2\tilde{m}G_{32}l^2, \tilde{d}_{62} = 2\tilde{m}G_{32,z}\ l^2, \tilde{d}_{63} = \left[-2\tilde{m}\tilde{m}^2G_{32} + 2\tilde{m}\tilde{n}^2G_{13} - 2\left(\tilde{m}^3 + \tilde{m}\tilde{n}^2\right)G_{21}\right]l^2,$$

$$\tilde{d}_{64} = \left[-2\tilde{m}\tilde{m}^2G_{32,z} + 2\tilde{m}\tilde{n}^2G_{13,z}\right]l^2, \tilde{d}_{65} = 2\tilde{n}G_{13}l^2, \tilde{d}_{66} = 2\tilde{n}G_{13,z}\ l^2,$$

$$\tilde{d}_{67} = \left[2\tilde{m}^2\tilde{n}G_{32} - 2\tilde{m}^2\tilde{n}G_{13} - 2\left(\tilde{m}^2\tilde{n} + \tilde{n}^3\right)G_{21}\right]l^2, \tilde{d}_{68} = \left[2\tilde{m}^2\tilde{n}G_{32,z} - 2\tilde{m}^2\tilde{n}G_{13,z}\right]l^2,$$

$$\tilde{d}_{69} = -2\left(\tilde{m}^2G_{32} + \tilde{n}^2G_{13}\right)l^2, \tilde{d}_{610} = -2\left[\tilde{m}^2G_{32,z} + \tilde{n}^2G_{13,z}\right]l^2, \tilde{d}_{611} = 2\left(\tilde{m}^4 + 2\tilde{m}^2\tilde{n}^2 + \tilde{n}^4\right)G_{21}l^2.$$